Chromogranin A preferential interaction with Golgi phosphatidic acid induces membrane deformation and contributes to secretory granule biogenesis

Ophélie Carmon, Fanny Laguerre, Lina Riachy, Charlène Delestre-Delacour, Qili Wang, Emeline Tanguy, Lydie Jeandel, Dorthe Cartier, Tamou Thahouly, Anne-Marie Haeberlé, et al.

Chromogranin A preferential interaction with Golgi phosphatidic acid induces membrane deformation and contributes to secretory granule biogenesis

Ophélie Carmon[1†], Fanny Laguerre[1†], Lina Riachy[1†], Charlène Delestre-Delacour[1£], Qili Wang[2], Emeline Tanguy[2], Lydie Jeandel[1], Dorthe Cartier[1], Tamou Thahouly[2], Anne-Marie Haeberlé[2], Laetitia Fouillen[3], Olivier Rezazgui[4], Damien Schapman[5], Alexandre Haefelé[4], Yannick Goumon[2], Ludovic Galas[5], Pierre-Yves Renard[4], Stéphane Alexandre[6], Nicolas Vitale[2§], Youssef Anouar[1§] and Maité Montero-Hadjadje[1§*]

[1] Normandie Univ, UNIROUEN, INSERM, U1239, Laboratoire de Différenciation et Communication Neuronale et Neuroendocrine, Institut de Recherche et d'Innovation Biomédicale de Normandie, 76000, Rouen, France

[2] Centre National de la Recherche Scientifique, Université de Strasbourg, Institut des Neurosciences Cellulaires et Intégratives, F-67000 Strasbourg, France

[3] Laboratoire de Biogénèse Membranaire, UMR-5200 CNRS, Plateforme Métabolome, Université de Bordeaux, 33883 Villenave D'Ornon, France

[4] Normandie Univ, UNIROUEN, COBRA, UMR 6014 and FR 3038, INSA Rouen, CNRS, 76000 Rouen, France

[5] Normandie Univ, UNIROUEN, INSERM, PRIMACEN, 76000, Rouen, France

[6] Normandie Univ, UNIROUEN, CNRS, UMR 6270, Polymères, Biopolymères, Surfaces Laboratory, 76000, Rouen, France

[†] These authors equally contributed to this work.

[£] Present address: Normandie Univ, UNIROUEN, Laboratoire GLYCOMEV, Fédération de recherche Normandie-Végétal - FED 4277, GDR CNRS 3711 COSM'ACTIFS, 76000, Rouen, France

[§] These authors equally contributed to this work.

[*] Corresponding author; Tel: +33 235146643; e-mail: maite.montero@univ-rouen.fr

RUNNING TITLE: CgA/PA interaction and granulogenesis

NONSTANDARD ABBREVIATIONS

AFM: atomic force microscopy

CgA: chromogranin A

CgB: chromogranin B

DOPC: 1,2-dioleoyl-sn-glycero-3-phosphocholine

FIPI: 5-Fluoro-2-indolyl des-chlorohalopemide

*g*CW STED: time-gated continuous wave stimulated emission depletion

GUV: giant unilamellar vesicle

ITC: isothermal titration calorimetry

PA: phosphatidic acid

PABD: PA binding domain

PC: phosphatidylcholine

PE: phosphatidylethanolamine

PS: phosphatidylserine

PDE4A1: cAMP phosphodiesterase-4A1

PLD: phospholipase D

SgII: secretogranin II

Spo20p: Sporulation-specific protein 20

SUV: small unilamellar vesicle

TGN: *trans*-Golgi network

ABSTRACT

Chromogranin A (CgA) is a key luminal actor of secretory granule biogenesis at the *trans*-Golgi network level but the molecular mechanisms involved remain obscure. Here, we investigated the possibility that CgA acts synergistically with specific membrane lipids to trigger secretory granule formation. We show that CgA preferentially interacts with the anionic glycerophospholipid phosphatidic acid (PA). In accordance, bioinformatic analysis predicted a PA-binding domain (PABD) in CgA sequence that effectively bound PA (36:1) or PA (40:6) in membrane models. We identified PA (36:1) and PA (40:6) as predominant species in Golgi and granule membranes of secretory cells and we found that CgA interaction with these PA species promotes artificial membrane deformation and remodeling. Furthermore, we demonstrated that disruption of either CgA PABD or phospholipase D (PLD) activity significantly alters secretory granule formation in secretory cells. Our findings show for the first time the ability of CgA to interact with PLD-generated PA, which allows membrane remodeling and curvature, key processes necessary to initiate secretory granule budding.

KEY WORDS: membrane dynamics / organelle biogenesis / phospholipase D / Golgi apparatus

INTRODUCTION

Secretory granules are vesicular organelles which materialize the regulated secretory pathway, allowing release of signal molecules such as hormones and neurotransmitters from endocrine, neuroendocrine, and most neuronal cells. Secretory granules are formed by budding from the trans-Golgi network (TGN) membrane in a very efficient manner and more than several thousand can accumulate in neuroendocrine cells for active release upon cell stimulation, most likely involving a specific budding process from the Golgi apparatus (1). It is now well established that membrane remodeling at the TGN is an important process for secretory granule budding, but the identity of the molecular actors, the sequence of events, and the mechanisms involved are not elucidated to date.

The TGN membrane is composed of a broad spectrum of lipids with specific properties that profoundly define its identity and function (2), but their contribution to secretory granule biogenesis has only recently emerged. Membrane proteins are known to influence lipid organization and conversely protein function and clustering are also under the control of lipids, leading to the formation of TGN membrane microdomains that have been proposed to regulate the budding of secretory granules (3). For instance, *in vitro* and *in vivo* studies revealed that depletion of cholesterol alters secretory granule biogenesis (4, 5), and the regulated production and organization of sphingomyelin, which assembles with cholesterol to generate microdomains in the membranes, has been shown to be crucial for the biogenesis of cargo carriers at the Golgi membranes (6). Moreover, the TGN membrane cytosolic leaflet is highly enriched in phosphatidylinositol 4-phosphate (PI4P), which may directly induce membrane curvature and/or recruit membrane-deforming cytosolic PI4P-binding proteins (7). Thus, besides the TGN membrane components, cytosolic but also luminal molecular components potentially influence membrane organization and shape. Among the luminal components, several glycoproteins of the granin family were proposed to play a crucial role in secretory granule biogenesis (8). In particular, chromogranin A (CgA) was shown to contribute to hormone aggregation and secretory granule biogenesis (9–11). Indeed, deletion of the CgA gene (*Chga*) led to decreased secretory granule number associated to metabolic complications such as cardiovascular defects and obesity in knockout mice (12, 13), implying a major contribution of CgA in catecholamine and insulin storage and release. In previous studies, we have shown that ectopic CgA expression induced the formation of secretory granule-like structures in COS7 cells, which are normally devoid of secretory granules and granin expression (14, 15), confirming the important role of CgA in granulogenesis. These

observations suggested that CgA could act at the level of the TGN membrane to trigger the formation of secretory granules; however, the mechanism involved is still unknown.

The first indication for a role of CgA at the TGN level is related to its acidic nature which confers to this granin the ability to aggregate with neuropeptides and hormones in the luminal TGN condition (9). Besides these soluble aggregates, a fraction of CgA was found to be tightly associated with secretory granule membrane (16), suggesting that CgA/hormone aggregates might interact with the TGN membrane. Indeed, the conserved α-helical organization of CgA terminal regions which confers to the protein the ability to trigger secretory granule formation and to sort hormones to the regulated secretory pathway (11, 14), the faculty of CgA to regulate fusion pore expansion (17) and the widespread expression of this granin argue for a role of CgA in granulogenesis through direct interaction with membranes. In fact, CgA-derived peptides with the conserved α-helical conformation have been shown to interact with membrane lipids. For instance, the conserved N-terminal peptide of CgA named vasostatin I (hCgA1-76) interacts with phosphatidylserine in phospholipid monolayers (18) and cell surface (19), whereas the peptide catestatin (hCgA352-372) binds to phosphatidylcholine micelles (20). As it is now well established that lipid composition and properties define organelle identity and function, we explored the possibility that an interaction between CgA and specific lipids of the TGN membrane could promote secretory granule biogenesis. In this study, we observed that CgA interacts with phosphatidic acid (PA) and phosphoinositides in membrane models and that ectopic expression of a cytosolic probe which buffers Golgi PA in secretory cells impaired the formation of CgA-containing granules. Moreover, we found that CgA preferentially interacts with few PA species enriched in purified Golgi and secretory granule membranes *in vitro*, through a newly identified PA-binding domain (PABD). Using giant unilamellar vesicles (GUVs) enriched with Golgi and secretory granule PA species, we observed that CgA induces GUV membrane remodeling and deformation in a dose-dependent manner. Interestingly, deletion of the identified PABD in CgA significantly reduced secretory granule biogenesis. Finally, genetic and pharmacological evidence revealed that inhibition of phospholipase D (PLD), a major source of PA production in the Golgi, alters secretory granule formation in neuroendocrine cells.

MATERIALS AND METHODS

Cell culture and transfection

African green monkey kidney fibroblast-derived COS7 cells (American Type Culture Collection; CRL 1651), wild-type or stably expressing CgA developed previously (15) and mouse corticotrope-derived AtT20/DC16v-F2 cells (American Type Culture Collection; CRL 1795) were maintained in Dulbecco's Modified Eagle's Medium (DMEM, Gibco, Thermo Fisher Scientific) supplemented with 5% heat-inactivated and sterile-filtered fetal bovine serum (FBS, Sigma - Aldrich), 100 U ml^{-1} penicillin, 100 µg ml^{-1} streptomycin (Gibco, Thermo Fisher Scientific) and 300 µg ml^{-1} geneticin (G-418 sulfate, Life Technologies, Inc, UK) to maintain gene resistance selection, at 37°C in 5% CO_2. Rat pheochromocytoma PC12 cells (American Type Culture Collection; CRL 1721) were routinely grown in Dulbecco's Modified Eagle's Medium (DMEM, Gibco, Thermo Fisher Scientific) supplemented with 5% FBS, 10% sterile-filtered HyClone Donor Equine serum (GE Healthcare, Life Sciences), 100 U ml^{-1} penicillin, 100 µg ml^{-1} streptomycin (Gibco, Thermo Fisher Scientific) and 1% L-glutamine 100X (Gibco, Thermo Fisher Scientific), at 37°C in 5% CO_2. For immunofluorescence (IF) experiments, COS7-WT, PC12 and AtT20 cells were transfected with 0.8 µg of DNA encoding GFP-tagged human CgA (CgA-GFP), GFP-tagged human ΔPABD CgA (CgAΔPABD-GFP), GFP-tagged rat PDE4A1(PABD) (PDE4A1 WT) or GFP-tagged rat PDE4A1(mutated PABD) (PDE4A1 Mut), and 2 µl Lipofectamine 2000 (Invitrogen) per well (24-well plate) according to the manufacturer's protocol. Four or five hours after the beginning of transfection, the culture medium was replaced by supplemented DMEM, and cells were additionally cultured for 24–48 h. For Western blot experiments, COS7-WT and AtT20 cells were transfected with 4 µg of DNA encoding CgA-GFP or CgAΔPABD-GFP, and 8 µl Lipofectamine 2000 (Invitrogen) per well (6-well plate) according to the manufacturer's protocol. Four or five hours after the beginning of transfection, the culture medium was replaced by supplemented DMEM, and cells were additionally cultured for 48 h.

Plasmid constructs

Full-length CgA-GFP (pCgA-EGFP-N2) kindly provided by M. Courel (UPMC, Paris, France) was used to amplify the sequence of CgA-encoding region by PCR using the sense primer (5'-CTCGAGGCCACCATGCGCTCCGCCGCTGTCTCGGCTTCTT-3'), including an Xho1 restriction site (underlined bases), and the antisense primer (5'-

CCGCGGGCGCCCCGCCGTAGTGCCTGCA-3'), including a SacII restriction site before cloning into a pGEM-T vector (Promega, Charbonnières, France). Site-directed mutagenesis was conducted by using the QuickChange® II XL Site-Directed Mutagenesis Kit (Agilent technologies, Les Ulis, France) and specific primers (sense: 5'-CTCTCCTTCCGGGCCCGGGCCTACGAGGACAGCCTTGAGGCGGGCCTG-3'; antisense: (5'-CAGGCCCGCCTCAAGGCTGTCCTCGTAGGCCCGGGCCCGGAAGGAG AG-3') designed to remove the CgA PABD sequence (residues 364–381). The amplified mutated CgA (with deleted PABD region) was digested with the appropriate enzymes (Xho1 and SacII) and subcloned into the eukaryotic expression vector pEGFP-N2. All the constructs were verified by restriction enzyme digestion and DNA sequencing. PDE4A1 WT and PDE4A1 Mut constructs were described previously (21).

Animals

Pld1 knockout mice were described previously (22, 23). They were housed and raised at Chronobiotron UMS 3415. All experiments were carried out in accordance with the European Communities Council Directive of 24th November 1986 (86/609/EEC) and resulting French regulations. Accordingly, the CREMEAS local ethical committee approved all experimental protocols. Every effort was made to minimize the number of animals used and their suffering.

Proteins and antibodies

Recombinant CgA (human chromogranin A 19-457aa, His tag, *E. coli*, ATGP0323, Atgen global) was used for lipid strips and GUVs experiments. For CgA-Alexa488 coupling, all reactants and solvents were purchased from TCI-Chemicals and Alfa Aesar. CgA labeling was performed according to a modified version of a protocol reported in Chevalier et al. (24). First, 82 µl (1 eq.) of Alexa488 solution (2 mg ml^{-1} in anhydrous N, N dimethylformamide) were introduced into a 1 ml round-bottom flask. (O-(N-succinimidyl)-N,N,N',N'-tetramethyluronium tetrafluoroborate (70 µg, 1.2 eq.) and N,N-diisopropylethyl-amine (0.04 ml, 1.2 eq.) were added and the reaction medium was placed under argon, with magnetic stirring at RT during 1 h, to obtain the N-hydroxysuccinimidyl activated ester. A solution of 250 µg of CgA in PBS buffer (pH 7.2, 0.5 mg ml^{-1}, 1 eq.) was then slowly added dropwise in the reaction medium, for a ratio Alexa488/CgA 10/1. Reaction was carried out under argon, magnetic stirring and at RT overnight. Purification was performed using 10 kDa centrifugation filters (Spin-X® UF 500, CORNING) previously conditioned with PBS to

remove glycerol and other biocidal compounds. Labeled protein was collected in PBS buffer following 3 centrifugations of 10 min at 7,500 rpm. Grafting rate was evaluated by Western blot and UV-Vis spectroscopy (λabs = 494 nm), with a maximum labeling rate of 5.6 Alexa488 molecules per protein.

Primary antibodies used were goat polyclonal anti-CgA (sc-23556; Santa-Cruz Biotechnology inc.) (1:200), rabbit polyclonal anti-CgA (WE-14 (25)) (1:1,000), rabbit polyclonal anti-CgA (RV31.4 (14) (1:1,000), rabbit polyclonal anti-SgII (EM66 (26)) (1:1,000), goat polyclonal anti-CgB (sc-1489; Santa-Cruz Biotechnology inc.) (1:1,000), mouse monoclonal anti-GM130 (BDBiosciences) (1:1,000), mouse monoclonal anti-CALR (clone 1G11-1A9, Sigma-Aldrich) (1:1,000), mouse monoclonal anti-GLUD1 (clone 3C2, Sigma-Aldrich) (1:500), mouse monoclonal anti-golgin 97 (A21270; Invitrogen) (1:500), mouse monoclonal anti-α-tubulin (T5168, Sigma-Aldrich) (1:5,000). For IF, secondary antibodies used were Alexa 488-conjugated donkey anti-rabbit IgG; Alexa 594-conjugated donkey anti-mouse IgG (Invitrogen) (1:500). For Western blotting, anti-rabbit, anti-mouse and anti-goat secondary antibodies conjugated to horseradish peroxydase (Thermo Fisher Scientific) (1:5,000) were used.

Protein-lipid binding assay

Membrane lipid strips (P-6002, Echelon Biosciences) were saturated in PBS-T buffer (0.1% v/v Tween 20 in PBS) supplemented with 3% fatty acid-free BSA (Sigma-Aldrich) for 1 h at RT, and then incubated with 500 ng ml^{-1} recombinant human purified CgA diluted in this buffer for an additional hour at RT. After several washes with PBS-T, the membranes were incubated with anti-WE-14 antibody (1:1,000) 1 h at RT in the saturation buffer. After washing with PBS-T, membranes were incubated with a secondary antibody coupled to horseradish peroxydase (Thermo Fisher Scientific) and visualized by enhanced chemiluminescence. Densitometric analysis was performed to determine the relative affinity of CgA binding to various phospholipids.

Subcellular fractionation

Cells were collected in PBS and sedimented by centrifugation at 400 *g* for 5 min at 4°C. The cell pellet was disrupted by 5 pulls/pushes through a 21- and then a 25-gauge needle attached

234 to a syringe, in ice-cold buffer (0.32 M sucrose, 20 mM Tris-HCl, pH 8; 1 ml g^{-1} of cells). The
235 resulting lysate was centrifuged at 800 *g* for 30 min at 4°C.

236

Golgi membrane purification

The protocol used was adapted form that developed by Graham et al (27) for the isolation of Golgi membranes from cultured cells by flotation through a discontinuous sucrose gradient. Briefly, Golgi membranes are isolated from low-speed pellets traditionally referred to as the nuclear pellet; hence the upper layer of the pellets (containing plasma, ER and Golgi membranes) were suspended in 1.4 M sucrose. The homogenate was deposited on a succession of 2 ml 1.4 and 2.0 M sucrose cushions and then covered with 2 ml 1.2 and 0.8 M sucrose cushions and 10 ml 0.32 M sucrose cushion, all sucrose cushions containing 10 mM Tris-HCl at pH 7.4. The extracts were then centrifuged at 10,000 *g* for 18 h at 4°C. The different fractions were collected in hemolysis tubes and kept at -20°C. An aliquot of each fraction was used for the localization of Golgi apparatus by Western blot using specific antibodies to recognize plasma membrane, Golgi, nucleus, mitochondria and the endoplasmic reticulum.

Secretory granule purification

Post-nuclear supernatants were centrifuged at 20,000 *g* for 20 min at 4°C. Pellets containing dense core granules were centrifuged on a multi-step gradient of 1 to 2.2 M sucrose (1, 1.2, 1.4, 1.6, 1.8, 2 and 2.2 M sucrose; 5 ml steps), at 100,000 *g* for 12 h at 4°C. All gradient steps were collected from the top of the tube in 5 ml fractions, and analyzed by western blotting to identify the granule-containing fractions and to verify their degree of purification.

Lipidomic analysis

Total lipids from recovered Golgi and granule fractions were extracted by the method of Bligh and Dyer (28). Lipid extracts were resuspended in 50 µl of eluent A. Liquid chromatography coupled to tandem mass spectrometry (LC-MS/MS) analyses were performed with a MS model QTRAP® 6500 (Sciex) coupled to an LC system (1290 Infinity II, Agilent). Analyses were achieved in the negative (PA); nitrogen was used for the curtain gas (set to 15), gas 1 (set to 20) and gas 2 (set to 0). Needle voltage was at − 4, 500 without needle heating; the declustering potential was adjusted set at − 180 V. The collision gas was also nitrogen; collision energy is set to − 50eV. Reversed phase separations were carried out at 50°C on a Luna C8 150×1 mm column, with 100 Å pore size, 5 µm particles (Phenomenex, Torrance, USA). Eluent A was isopropanol/CH_3OH/H_2O+0.2 % formic acid+0.028 % NH_3

and eluent B was isopropanol+0.2 % formic acid+0.028 % NH_3. The gradient elution program was as follows: 0-5 min, 30-50 % B; 5 - 30 min, 50-80 % B; 31–41 min, 95 % B; 42–52 min, 30 % B. The flow rate was set at 40 µl min^{-1}; 3 µl sample volumes were injected. Quantitative PA analyses were made based on MS/MS multiple reaction monitoring (MRM) as described (29). Briefly, MRM transitions for individual PAs were determined using PA standards (Avanti Polar Lipids, Alabaster, USA). The predominant daughter fragment ions were then used for quantitative MRM analysis. MRM transitions and specific retention times were used to selectively monitor PA using MultiQuant software (v3.0, Sciex).

Liposome and giant unilamellar vesicle formation and use

Liposome flotation and binding assays

Lipids solubilized in chloroform were purchased from Avanti Polar Lipids (Alabaster, USA) and were used without further purification. Liposome mixtures were prepared in mass ratios composed of 90% DOPC (1,2-dioleoyl-*sn*-glycero-3-phosphocholine), 5% PE-NBD (1,2-dioleoyl-*sn*-glycero-3-phosphoethanolamine-N-(7-nitro-2-1,3-benzoxadiazol-4-yl)), and 5% PS (1,2-dioleoyl-sn-glycero-3-phospho-L-serine), $PI(4,5)P_2$ (1,2-dioleoyl-sn-glycero-3-phospho-(1'-myo-inositol-4',5'-bisphosphate)), egg PA mix or PA species (36:1 (1-stearoyl-2-oleoyl-*sn*-glycero-3-phosphate), 36:2 (1-stearoyl-2-linoleoyl-sn-glycero-3-phosphate), 40:6 (1-stearoyl-2-docosahexaenoyl-*sn*-glycero-3-phosphate) or 36:0 (1,2-distearoyl-sn-glycero-3-phosphate). Lipids were dried in a stream of nitrogen and kept under vacuum for at least 2 h. Dried lipids were then suspended in liposome-binding buffer (LBB: 20 mM HEPES, pH 7.4, 150 mM NaCl, 1 mM $MgCl_2$) by three freeze and thaw cycles and were extruded using a Mini-Extruder (Avanti Polar Lipids, Alabaster, USA) through polycarbonate track-etched membrane filters to produce liposomes of 200 nm in diameter. The liposomes were then diluted in LBB (1:10) and incubated with 30 µg of COS7-CgA extract during 20 min. Then, samples were centrifuged at 200,000 *g* (1 h at 4°C) on a multi-step gradient sucrose. To determine the association of CgA with liposomes, the fractions were collected after centrifugation, and the presence of CgA was revealed using western blot analysis of the different fractions.

To quantify liposome binding to GST-CgA-PABD linked to GSH-Sepharose beads, GST and GST-PABD constructs (330 pmol) bound to GSH beads were washed once with 1 ml of LBB medium before incubation for 20 min in the dark at room temperature and under agitation with liposomes containing a 10-fold molar excess of PA relative to the quantity of GST

proteins in a final volume of 200 µl of LBB. Beads were washed three times with 1 ml of ice-cold LBB and collected by centrifugation at 3,000 rpm for 5 min. Liposome binding to the PABD was estimated by measuring the fluorescence at 535 nm with a Mithras fluorimeter (Berthold). Triplicate measurements were performed for each condition. Fluorescence measured with GST linked to GSH-Sepharose beads alone was between 3 and 4 A.U. and was subtracted from sample measurements.

Giant unilamellar vesicle preparation

Giant unilamellar vesicles (GUVs) were prepared by polyvinyl acetate (PVA, MW 145000, purchased from VWR International, Fontenay-sous-Bois, France) – assisted swelling. Briefly, a Teflon plate was used and was cleaned twice with 99% ethanol. A 5% (w/w) solution of PVA was prepared by stirring PVA in water while heating at 90°C. PVA-coated substrates were prepared by spreading 100–300 µl of PVA solution on a clean Teflon plate, and dried for 30 min at 80°C. 10–20 µl of a lipid mixture (95% of DOPC, 4% of PA (36:1) or (40:6) and 1% of PE-NBD) dissolved in chloroform (1 mg ml^{-1}) was spread on the dried PVA film and placed under vacuum overnight at RT to evaporate the solvent. A chamber around the drops of lipids was formed with Vitrex and filled with 100 mM sucrose and 150 mM NaCl solution during 3 h at room temperature, allowing the formation of GUVs with a suitable size. Next, the buffer containing GUVs is recovered using a rib with a wide tip to avoid destroying the GUVs, and deposited in LabTek wells (LabTek I non-separable, on glass coverslip, 4 culture chambers, Nunc), which were previously coated with a 1 mg ml^{-1} BSA (Bovine Serum Albumin, Sigma – Aldrich) solution. To allow the sedimentation of GUVs, we added the same volume (100 µl) of a solution containing 90 mM glucose and 15 mM NaCl in LabTek wells. The sedimentation of the GUVs takes place for about 1 h at RT.

To test the effect of CgA on the GUV membranes, we added CgA or CgA-Alexa488 in GUV-containing Labtek wells at a final concentration of 2, 4 or 6 µM just before the beginning of confocal microscopy acquisitions.

Small unilamellar vesicle preparation

Small unilamellar vesicles (SUVs) were prepared using the standard extrusion method as described previously for liposome formation. Liposome mixtures repared in mass ratios composed of 90% DOPC, 10% PA (36:1) were dissolved in a test tube with chloroform. Lipids were dried under argon gaz. The lipid film thus obtained was hydrated with 500 µl of

water and the solution was subjected to vortex mixing for 1 h at room temperature. The multilamellar vesicles were extruded 27 times using the Mini-Extruder equipped with a polycarbonate membrane filter of 100 nm pore diameter to obtain SUVs.

Atomic force microscopy measurements

Membrane preparation

Giant Unilamellar Vesicles (GUVs) were prepared by using 100% DOPC or a mix of 90% DOPC and 10% PA (36:1). The vesicles were prepared in a 200 mM sucrose solution. GUV solution was diluted 100 times in 250 mM glucose solution to promote their sedimentation and to avoid multilayers. Final lipid concentration was 10 μM. The vesicle solution was injected in the AFM liquid cell and put in contact with freshly cleaved mica. After 2 min, the vesicle solution is replaced with 250 mM glucose solution in order to maintain the supported lipid bilayers hydrated at all times during imaging. To study protein/lipid interactions, the glucose solution was replaced with a CgA solution (0.6 or 1.2 μM), and the sample was imaged again.

Microscopy imaging

AFM measurements were performed on a multimode atomic force microscope (Nanoscope IIIA, Veeco, USA). Supported lipid bilayers images were taken in tapping mode in the fluid cell. A soft cantilever with a typical spring constant of 0.06 N/m and equipped with a silicon nitride tip was used. The tip velocity was set between 5-10 μm/s by varying the scan rate according to the scan size. The cantilever oscillation was tuned to a frequency between 20 and 30 kHz, and the amplitude was set between 0.8 V and 2 V. All the experiments were carried out at a temperature of 21°C.

High-sensitivity isothermal titration calorimetry

Isothermal titration calorimetry (ITC) was performed on an Affinity instrument (TA Instrument, New Castle, DE) equipped with a 185 μl reaction chamber. Solutions were degassed under low pressure before use to avoid the formation of air bubbles while titrating. The CgA solution (5 μM) was placed in the calorimeter chamber and SUV suspension (10 mM) was injected in aliquots of 2.5 μl. The period between two successive injections was typically 200 sec to allow the system to reach equilibrium. The solution was stirred

continuously at 125 rpm and the experiments were carried out at a temperature of 10°C. The resulting heat changes after SUV injection were recorded as a function of time. The heat of reaction was obtained by integrating the area under each peak of heat flow tracings, using the heat of SUV dilution in water as blank sample. The data were acquired by using the Nanoanalyze software (v.3.10.0, TA Instrument).

Immunofluorescence labelling

COS7-CgA cells were cultured in 24-well plates (Costar® 24 Well Clear TC-Treated Multiple Well Plates, Corning), onto glass coverslips and fixed with 4% paraformaldehyde (Sigma – Aldrich) in PBS at RT for 15 min. Cells were permeabilized and blocked for 30 min with 0.3% Triton X-100 (Thermo Fisher Scientific), in PBS containing 5% normal donkey serum (Sigma – Aldrich) (1:50) and 1% BSA. Cells were then incubated for 2 h at RT with primary antibodies, and, after washing with PBS, for 1 h with secondary antibodies. Nuclei were stained with DAPI (4',6-diamidino-2-phenylindole, Molecular probes) (1 µg ml^{-1}). To verify the specificity of the immunoreactions, the primary or secondary antibodies were substituted with PBS.

Protein electrophoresis and Western blotting

Cells were harvested by scraping in NP40 cell lysate buffer (Thermo Fisher Scientific) supplemented with a cocktail of protease inhibitors (Thermo Fisher Scientific), homogenized, and proteins were separated by SDS-PAGE followed by Western blotting. Membranes were incubated in a blocking buffer containing 5% non-fat dry milk in PBS containing 0.5% Tween 20 (Sigma - Aldrich) (PBS-T) for 1 h at RT, and overnight with primary antibodies at 4°C. Then, membranes were washed for 45 min with PBS-T. Blots were subsequently incubated for 1 h with appropriate HRP (Horse Radish Peroxidase)-conjugated secondary antibody (Thermo Fisher Scientific) in blocking buffer. Membranes were washed for 45 min with PBS-T and immunoreactive proteins were detected by chemiluminescence (BioRad Biotechnology). Quantification was performed using Image Lab software (5.0 build 18, 2013 version, Bio-Rad Laboratories). The mean intensity of each individual band of interest was calculated after background value subtraction.

Image acquisition

For GUVs experiments, real-time videomicroscopy was carried out with an inverse confocal microscope TCS-SP5 AOBS (*Acousto-Optical Beam Splitter*), equipped with pulsed white light laser (WLL) and with a 63X oil immersion objective (Leica Microsystems). PE–NBD was excited at 463 nm and observed in a 510-550 nm window. Images were acquired at a speed of one frame per 2 s during 1 min.

For immunocytochemistry experiments, confocal microscopy was carried out with a TCS-SP8 upright confocal laser-scanning microscope equipped with 63X oil immersion objective (NA=1.4; Leica, Microsystems). Alexa 488 and GFP were excited at 488 nm and observed in a 505–540 nm window. Alexa 594 was excited at 594 nm and observed in a 600–630nm window. For dual color acquisition, images were sequentially acquired in line scan mode (average line = 2). Overlays were performed with post acquisition Leica Confocal Software functions to obtain the presented snapshots.

For super-resolution experiments, image acquisitions were performed with a 100X oil immersion objective (NA 1.4) through time-gated continuous wave stimulated emission depletion (*g*CW STED) imaging (TCS SP5-X; Leica Microsystems) (30) with optimized parameters for GFP detection (Supplemental Fig. 2). Samples (zoom 8, pixel size = 18.95 nm) were excited with a 488 nm wavelength of a supercontinuum laser (20–30% AOTF). A conventional scanner (400 Hz, Line Average 1, Frame Average 1, Frame Accumulation 3, 1024 × 1024) was used. Depletion was obtained with a 592 nm laser (70% AOTF). Fluorescence (500–550 nm) was collected with a hybrid detector (Gain 100) in the gated mode and a pinhole for Airy 1.

Transmission electron microscopy of WT and *Pld1*$^{-/-}$ chromaffin cells in situ

WT and *Pld1*$^{-/-}$ mice were anesthetized with a mixture of ketamine (100 mg kg^{-1}) and xylazine (5 mg kg^{-1}) and transcardiacally perfused with 0.1 M phosphate buffer, pH 7.3, containing 2% paraformaldehyde and 2.5% glutaraldehyde. The 2-mm-thick slices were cut from the adrenal glands and postfixed in 1% glutaraldehyde in phosphate buffer overnight at 4°C. The slices were then immersed for 1 h in OsO4 0.5% in phosphate buffer. 1-mm^3 blocks were cut in the adrenal medulla, dehydrated, and processed classically for embedding in Araldite and ultramicrotomy. Ultrathin sections were counterstained with uranyl acetate and examined with a Hitachi 7500 transmission electron microscope.

Post-acquisition analysis

The following procedure was used to measure the number of CgA granules. The confocal section generated by the Leica TCS-SP8 confocal microscope was analyzed with Imaris and converted into an Imaris file. A broad region of interest (ROI) was defined around a cell. Then with the tool 'spots detection' on Imaris, the number of spots with a diameter > 200 nm was quantified. Spots statistics are automatically computed for each spot object. It provides a procedure to automatically detect point-like structures, an editor to manually correct detection errors, a viewer to visualize the point-like structures as spheres, and statistics output.

To analyze secretory granule density in wild-type (WT) and *Pld1* knock-out chromaffin cells, secretory granules were counted in 50 chromaffin cells from WT and *Pld1* KO mice with a visible nucleus randomly selected in ultrathin sections from several blocks (1 section/block) from each mouse (n=3 mice per genotype). Dense core diameter was measured from 950 randomly selected granules for each genotype using the line segment tool of Image J. To minimize the bias measurements, samples were blinded.

To improve signal-to-noise ratio in STED images, deconvolution of raw data was obtained through image processing with Huygens professional 4.5.1 software (SVI, The Netherlands) (31).

Statistics

Data were analyzed with the Prism program (GraphPad 6.04 Software). For the quantification of the number of CgA granules in IF studies, statistical significance was determined by Mann-Whitney U test. Values are expressed as means ± s.e.m. or S.D., and the level of significance is designated in the figure legend as follows: * $P<0.05$, ** $P<0.01$, *** $P<0.001$. For the quantification of CgA signal in lipid strip experiments, statistical significance was determined by an Anova one-way analysis of variance test with Bonferroni's comparison test. Values are expressed as means ± s.e.m., and the level of significance is designated in the figure legend as follows: *** $P<0.001$. For the quantification of membrane deformation after CgA addition on GUVs, statistical significance was determined by Mann-Whitney U test. Values are expressed as means ± s.e.m., and the level of significance is designated in the figure legend as follows: *** $P<0.001$. For the quantification of the number of secretory granules and their dense core diameter in MET study, statistical significance was determined by Mann-Whitney U test. Values are expressed as means ± s.e.m., and the level of significance is designated in the figure legend as follows: * $P<0.05$.

465

RESULTS

Chromogranin A interacts preferentially with PA

Due to the presence of two helicoidal motives in its N- and C-terminal conserved regions which bear the granulogenic activity of CgA and which can promote binding to lipids (11), we analyzed the capacity of the granin to interact with membrane lipids. A lipid overlay assay was performed by incubating recombinant CgA with a nitrocellulose sheet where different membrane lipids were adsorbed. Using an antibody raised against CgA (25), this overlay assay revealed that CgA interacts with PA and phosphoinositides (PIP, PIP_2 and PIP_3) (Fig. 1 A). Quantification of the CgA-lipid interaction signals revealed that CgA preferentially interacts with PA (Fig. 1 A).

Golgi PA is involved in the biogenesis of CgA-containing secretory granules

To examine the importance of PA in the formation of CgA-induced secretory granules, we overexpressed the PABD of the cytosolic phosphodiesterase PDE4A1 in neuroendocrine PC12 cells in order to reduce the ability of CgA to interact with PA in Golgi membranes. Indeed, PDE4A1 PABD was previously shown to interact with PA specifically at the TGN in COS1 cells (32) and RAW264.7 macrophages (21), and its overexpression should reduce the amount of available PA at this level. We found that PDE4A1(PABD) not only exhibited the expected Golgi-like confined localization, but also significantly reduced the number of CgA secretory granules, without affecting CgA expression (Fig. 1 B). Moreover, expression of PDE4A1(PABD Mut) which does not bind to PA and which was not detected in the Golgi area did not impair the biogenesis of CgA-induced granules (Fig. 1 B), strongly supporting the crucial role of Golgi PA in the formation of CgA secretory granules.

Chromogranin A interacts with PA through a putative PA-binding domain

To characterize the CgA region involved in PA binding, we compared the CgA helicoidal motifs with those of proteins with known PABD, notably the Golgi PA-binding protein PDE4A1. This analysis revealed a potential PABD within residues 352-381 of CgA, a sequence containing positively charged and hydrophobic amino acids (Fig. 1 C). Indeed, a bioinformatics analysis using Heliquest software (33) further refined this PABD to residues 364 - 381 (Fig. 1 C), which shares the characteristics of typical PABDs (34). It is predicted that this PABD adopts an amphipathic α-helical conformation with five positively charged

residues (arginines) sequestered in one side of the helix, which could interact with the negatively charged polar head of PA, and three surface exposed hydrophobic residues (tryptophane, phenylalanine, leucine) on the other side of the helix which could insert within the hydrophobic part of membranes and interact with the fatty acid chains of PA (Fig. 1 D). Interestingly, a 3D structural model of CgA PABD confirmed that this domain displays an α-helix when its structure was examined using MacPyMol software (shown as a ribbon, Fig. 1 E). We then used a semi-quantitative *in vitro* assay with NBD-labeled liposomes (21) to investigate the PA binding capacity of three different GST fusion proteins containing the C-terminal helicoidal motif of CgA or parts of it: CgA(352-381) (CgA PABD), CgA(352-372) (catestatin) and CgA(373-381). We found that GST-CgA(352-381) very efficiently bound PA-containing liposomes, while the binding of GST-CgA(352-372) was greatly reduced and that of GST-CgA(373-381) was even lower (Fig. 1 F). In contrast, none of the proteins tested efficiently bound PC NBD-liposomes (Fig. 1F), highlighting the preferential affinity of the CgA α-helix for PA rather than for curved membranes. These data not only indicate that the entire sequence corresponding to CgA PABD is important for PA binding but also that CgA proteolysis, as it occurs in secretory granules and which generates the peptide catestatin (CgA(352-372)) (Fig. 1 C), should disrupt this binding.

Specific PA species are predominant and common to Golgi and secretory granule membranes from CgA-expressing cells

We analyzed and compared the PA content of Golgi and secretory granule membrane fractions purified from COS7 cells stably expressing CgA (COS7-CgA). These cells display CgA-containing secretory granule-like structures in contrast to their WT counterparts with no CgA (14, 15). The enrichment of secretory granule and Golgi membrane fractions was evaluated by western blotting (Supplemental Fig. 1). Detailed lipidomics analysis of these fractions revealed that over the 44 distinct species detected, only few specific PA species are predominantly identified in secretory granule and Golgi membranes of COS7-CgA cells, *i.e.* PA (36:1), PA (38:2), PA (38:6) and PA (40:6) (Fig. 2 A). Furthermore, we compared the Golgi membrane of COS7-WT and COS7-CgA cells to examine the potential impact of CgA expression on the PA content. We found that the Golgi membrane of COS7-WT and COS7-CgA cells exhibit the same predominant PA species, *i.e.* PA (36:1), PA (38:2) and PA (40:6), but we also noticed a significant enrichment in PA (36:1) in Golgi membranes after CgA expression, mainly at the expense of PA (40:6) (Fig. 2 B). The presence of the same major PA

species, namely PA (36:1), PA (38:2) and PA (40:6), was also found in secretory granule membranes isolated from the neuroendocrine PC12 cells (Fig. 2 C). These data suggest that PA (36:1), PA (38:2) and PA (40:6) could represent crucial species for secretory granule formation.

Chromogranin A interacts with major Golgi/secretory granule PA species included in giant liposomes and induces membrane deformation and vesicle budding

To test the interaction between CgA from COS7-CgA cell extracts and the predominant PA species identified in Golgi and secretory granule membranes, we used a liposome flotation assay (Fig. 3 A). Following the flotation assay, the different fractions were analyzed by western blotting using a CgA specific antibody (25). This analysis revealed a strong interaction between CgA and liposomes enriched with PA species identified previously by lipidomics analysis, with an apparent preference for PA (36:1), and far less interaction with PIP_2-enriched liposomes (Fig. 3 B). In contrast, no interaction was found with liposomes enriched with phosphatidylcholine (PC), phosphatidylserine (PS) or PA (36:0), in accordance with the results obtained using lipid strips (Fig. 1 B; Fig. 3 B). These results demonstrate that endogenous CgA interacts specifically with predominant PA species identified in Golgi and secretory granule membranes from CgA-expressing cells.

To examine the membrane dynamics following CgA and PA interaction, we developed a model of GUVs enriched in PA (36:1) or PA (40:6), whose formation is assisted by a polyvinyl alcohol gel. To analyze their morphology using confocal microscopy, we generated PA-enriched GUVs containing a fluorescent lipid, phosphatidylethanolamine (PE)-NBD. After image acquisitions, we observed that the formed GUVs exhibit a diameter ranging between 5 and 50 μm, that the fluorescence is homogeneously distributed around the GUVs and that there are no budding events (Fig. 3 C; supplemental video 1). Addition of 2 μM CgA to PA-enriched GUVs provoked a marked fluorescence concentration in confined membrane domains of several GUVs just before budding events which resulted in the formation of small vesicles (Fig. 3 D; supplemental video 2). Quantification of membrane deformations generating vesicles revealed that the number of budding events depends on CgA concentration (Fig. 3 E). Finally, to analyze the direct involvement of CgA in GUV membrane remodeling, we generated a CgA fluorescent probe, CgA-Alexa488, and we observed that addition of 2 μM CgA-Alexa488 on non-fluorescent PA-enriched GUVs results first in a rapid and homogenous fluorescence distribution in GUV membranes, and then

within a minute budding events were detected in fluorescent CgA-enriched membrane domains (Fig. 3 F). Altogether, these results indicate that CgA interacts with membrane PA and that this interaction could induce a membrane remodeling resulting in vesicle budding.

Thermodynamic characteristics of CgA/PA interaction indicate that PA favors CgA incorporation in liposome membranes

To investigate the CgA/PA interaction in more details, we conducted an ITC analysis, which quantifies the binding equilibrium directly by measuring the heat change resulting from the association of a ligand with its binding partner (35, 36). ITC thermograms showed that injection of a water suspension of small unilamellar vesicles (SUVs) composed of 1,2-dioleoyl-sn-glycero-3-phosphocholine (DOPC) or DOPC/PA (36:1) induced an exothermic process resulting from the dilution process of SUVs in water (Fig. 4, A and B, upper panels). When we injected DOPC or DOPC/PA (36:1) SUV suspension into a CgA solution, the ITC results showed sequential exothermic and endothermic processes (Fig. 4, A and B, lower panels). Enthalpy curves (Fig. 4 C) were obtained from the integrated energy values obtained from A and B traces in lower panels, using A and B traces in upper panels as blank, respectively. These curves were fitted using two simple one-site binding model to yield thermodynamic parameters (Table 1). Comparing the enthalpy curves obtained after DOPC and DOPC/PA (36:1) injection in CgA solution, we observed an increase due to an exothermic process related to the binding of CgA with DOPC that could result from hydrogen bonding and/or electrostatic force (18). We also noticed that the maximum of enthalpy is reached after 14 injections of DOPC SUVs while it is reached only after 6 injections of DOPC/PA (36:1) SUVs (Fig. 4 C). In addition, for the exothermic process, the calculated enthalpy ratio $\Delta H^{exo}_{DOPC/PA(36:1)}/\Delta H^{exo}_{DOPC}$ is close to 7, the enthalpy ratio $\Delta H^{endo}_{DOPC/PA(36:1)}/\Delta H^{endo}_{DOPC}$ is equal to 12, and the stoichiometry (n) for both processes is lower with DOPC/PA (36:1) SUVs (Table 1). Moreover, the endothermic phase leads to enthalpy decrease (Fig. 4 C) and the stoichiometric ratio, which is the ratio between the total number of lipids and the number of lipids on the outer surface of the SUV, is close to 1.8, suggesting a reorganization of the protein/lipid complex in the SUV membrane. Together, these results clearly show that PA favors the incorporation of CgA in the SUV membrane.

Chromogranin A induces the remodeling of supported membrane bilayers enriched with Golgi/secretory granule PA

Using atomic force microscopy (AFM), we studied the impact of CgA on supported bilayers composed of DOPC or DOPC/PA (36:1). Addition of 0.6 or 1.2 µM CgA during 15 min (T1) and 75 min (T2) on DOPC membranes revealed small alterations of their topographical profile corresponding to protrusions with a maximal height of 4 nm (Fig. 5 A). In contrast, addition of 0.6 or 1.2 µM CgA on DOPC/PA (36:1) membranes led to local profile changes of the membrane with a height of the protrusions above 4 and 16 nm, respectively (Fig. 5 B). Of note, the grain size analysis of 11-15 images obtained with 1.2 µM CgA during 75 min revealed that the total number of CgA-induced domains increases by a factor of 3 after PA (36:1) addition in DOPC bilayers (41±23 domains per 100 μm^2 DOPC bilayer (Fig. 6 A) versus 120±41 domains per 100 μm^2 DOPC/PA (36:1) bilayer (Fig. 6 B)). Moreover, domains with an area greater than 20 μm^2 were clearly more abundant in presence of PA (36:1) in the supported bilayer, and their height increased with their area to reach a mean of 21±3 nm (Fig. 6 B). These results suggest that CgA interacts with PA-enriched lipid bilayers and that this interaction modifies membrane topology, in a concentration and time-dependent manner.

Chromogranin A PABD is required for secretory granule biogenesis

To analyze the role of the predicted CgA PABD in the formation of secretory granules, we expressed CgA where the PABD was deleted (CgAΔPABD-GFP) in COS7 and AtT20 cells. This specific CgA alteration significantly reduced secretory granule formation as compared to native CgA (Fig. 7, A and B). Indeed, although CgAΔPABD-GFP and CgA-GFP both colocalized with the Golgi marker GM130, the number of CgA positive granules is reduced when the PABD is deleted from CgA in COS7 cells (Fig. 7 A), but also in ATt20 cells although transfection efficiency was lower (Fig.7 B). Using deconvoluted time-gated continuous wave stimulated emission depletion (*g*CW STED) nanoscopy to overcome the noise at the Golgi level (Supplemental Fig. 2), we confirmed a reduction of CgA-containing structures in the Golgi area of both cell types expressing CgAΔPABD-GFP (Fig. 7, C and D). Altogether, these results support the idea that the interaction of CgA with PA through its PADB is important for granule biogenesis.

Inhibition of PLD-mediated PA synthesis alters the biogenesis of secretory granules

To study the implication of PA in Golgi membranes during the biogenesis of CgA-containing secretory granules, we altered PLD-mediated PA synthesis since PLD appears to be the most important provider of PA in the Golgi (37). First, secretory cells were incubated with the PLD pan-inhibitor FIPI, which provoked a significant reduction in the number of CgA-containing granules in COS7-CgA cells (Fig. 8 A) and a smaller reduction in PC12 cells (Fig. 8 B), without any apparent effect on the levels of three major granins (CgA, CgB, SgII). Interestingly, in chromaffin cells obtained from mice lacking *Pld1* gene (*Pld1*$^{-/-}$), we observed by electron microscopy a significant reduction in the number of secretory granules (Fig. 8, C and D), associated to a decrease in their dense core diameter (Fig. 8, C and E). Thus, pharmacological and genetic invalidation of PLD activity and expression supported the notion that PLD1 is an important provider of PA in Golgi membranes (38), and showed that PLD1-generated PA is required for the biogenesis of secretory granules containing CgA.

DISCUSSION

Although considerable efforts have been deployed to identify the molecular mechanism at the origin of secretory granule formation, many aspects of this fundamental process remain to be elucidated. The biogenesis of secretory granules depends on TGN membrane dynamics that rely on interactions of cytosolic and luminal proteins with molecular components of the TGN membrane. Among TGN luminal proteins, members of the granin protein family have been long considered as major actors of secretory granule biogenesis but direct mechanistic evidence is still lacking (39).

Here, we first uncovered the ability of the coiled-coil glycoprotein CgA to bind acidic phospholipids, in particular PA, using a lipid-overlay assay. Since PA was suspected to play a role in secretory granule biogenesis (40), we overexpressed the cytosolic phosphodiesterase PDE4A1, a *bona fide* PA binding protein in Golgi membranes characterized previously (21) to test this possibility. We observed a decrease in the number of CgA-containing secretory granules in PC12 cells in the presence of PDE4A1-PABD, presumably acting as a competitor for endogenous PA, suggesting that luminal CgA requires TGN membrane PA to generate secretory granules. As most enzymes involved in PA synthesis are found in the cytoplasmic leaflet of intracellular membranes, it is expected that most PA is generated in these membrane cytosolic leaflets. However, passive PA flip/flop or active PA-transfer by flippase, floppase and scramblase could efficiently alter this translayer asymmetry for PA. Accordingly, we

observed that PA was readily detected on the inner leaflet of the plasma membrane of PC12 cells expressing the PA binding protein Spo20p-GFP less than one minute after cell incubation with 10µM of PA micelles (unpublished observation). Additionally, *in vitro* experiments have suggested that intrinsic flipping of PA is affected by various parameters including pH and the geometry of specific PA species (41, 42). Thus, it is likely that significant levels of PA are present in the luminal leaflet of the TGN and therefore CgA/PA interaction could be effective at this location.

In silico identification of the CgA(364-381) sequence as a PABD further supported the possibility of CgA/PA interaction, which was confirmed using PA-enriched liposomes, as this sequence specifically binds PA. Interestingly, CgA PABD binds PA at a level similar to that observed for PDE4A1. In contrast, shorter fragments, corresponding to the expected cleavage of CgA occurring during secretory granule maturation to generate catestatin, exhibited only a weak interaction with PA. We can therefore anticipate that CgA/PA interaction might be regulated during secretory granule maturation and CgA processing. It is tempting to speculate that CgA and PA interact early in the TGN to trigger secretory granule formation, but that this interaction is disrupted later by proteolysis after budding to generate catestatin and to ensure secretory granule homeostasis. Such a sequential role has previously been demonstrated for the granin 7B2 in the regulation of the proteolytic enzyme PC2 and hormone sorting and secretion in endocrine cells (43). Moreover, the CgA PABD sequence may allow hydrophobic residue insertion into lipid bilayers and direct ionic interaction between basic residues and several PA molecules. Thus, CgA may participate to TGN remodeling by interacting with TGN predominant PA species that could induce the formation of PA-enriched microdomains. Indeed, CgA represents 40 to 80% of the protein content of secretory granules in chromaffin cells and the concentration is in the order of millimolar, representing around 5,000 CgA molecules per granule (44, 45). On the other hand, molecular dynamic simulation of the interaction of PA with the yeast protein Spo20p PABD revealed that up to 6 PA molecules bind to one Spo20p molecule (46). Based on the number of positively charged residues in the CgA PABD, it is possible that one CgA binds and sequesters up to 5 PA. Therefore, this can yield an extremely high density of PA, with up to 25,000 molecules accumulating with CgA on specific locations of the inner leaflet of the TGN membrane. Accumulation of the conical-shaped PA enables membrane bending (47), and this phenomenon could generate TGN membrane curvature preceding secretory granule budding.

To further support the role of PA in secretory granule formation, we analyzed and compared the PA composition in Golgi and secretory granule membranes from COS7-CgA cells by mass spectrometry, and found a strong similarity in the PA species present in the membranes of these two compartments. Among these PA species, we observed a predominance of several common mono- and poly-unsaturated forms, *i.e.* PA (36:1) and PA (40:6). Interestingly, these PA species were also identified in the membrane of secretory granules from neuroendocrine PC12 cells, suggesting that specific PA species occur at the Golgi membrane of CgA-expressing cells to induce the biogenesis of secretory granules, and that one or some of these species have a key role in this process. Using liposome models enriched with distinct phospholipids, we observed that CgA preferentially interacts with PA (36:1) and PA (40:6), and that addition of this granin generates deformation of PA (36:1)- or PA (40:6)-enriched artificial membranes in a dose-dependent manner. Of note, budding occurs in an outward direction from PA-enriched giant liposome membrane towards CgA, contrasting with the required budding towards the cytosol required for secretory granule formation. This apparent discrepancy is probably due to the fact that native membranes are more complex than artificial membranes in terms of lipid variety and asymmetric distribution between the two leaflets, in addition to the presence of other membrane proteins and the impact of cytosolic and luminal membrane environment (pH, ion concentration, cytosolic proteins). The hydrophobic face of CgA PABD helix was proposed to partially insert into artificial membrane, stressing nearby lipid packing, creating local defects, and promoting membrane curvature. In any case, the fact that generated buds stay attached to the GUV surface is consistent with the absence of cytosolic proteins involved in vesicle fission, such as dynamin. The analysis of the thermodynamic characteristics of CgA/PA (36:1) interaction by ITC consolidated the observation that CgA strongly interacts with PA (36:1)-enriched membranes to promote membrane deformation. Atomic force microscopy on supported membrane bilayers revealed that PA (36:1) enrichment increased the number, the height and the surface of CgA-induced domains resulting from either CgA aggregation, membrane deformation, microdomain formation, or any combination of these. These data support a central role for PA in the formation of CgA-induced domains as observed by confocal microscopy and ITC. Altogether, these results are in line with the idea that CgA/PA (36:1) or PA (40:6) interaction could play a key role in the membrane remodeling process necessary for secretory granule budding.

In accordance, we showed that expression of CgA deprived from its PABD leads to a significant decrease in the number of CgA granules, with a reduction of CgA granule number in whole cell but also in the Golgi area. The CgA-PABD deletion mutant is apparently acting as a negative-dominant impairing CgA-induced granule formation, probably by disrupting the molecular interactions normally occurring between CgA and PA at Golgi membranes. Therefore, these data support the notion that CgA-PABD is involved in granule biogenesis and that CgA/PA interaction through this domain is critical for the initiation of the secretory process in neuroendocrine cells. Interestingly, the C-terminal sequence of catestatin (CgA(352-372)) including the PABD contains several single nucleotide polymorphisms associated with metabolic and cardiovascular disorders in humans (48, 49), suggesting a potential link between the onset of these diseases and the disruption of hormone release related to an alteration of CgA secretory granule biogenesis.

Moreover, several studies demonstrated that the enzymatic activity of PLD1 converting PC to PA is an important source of Golgi PA (38), which is required for secretory granule budding (50), but also involved in secretory granule fusion with the plasma membrane (51). Pharmacological inhibition of PLD in COS7-CgA and PC12 cells, and *Pld1* knockout in mouse chromaffin cells, both reduced secretory granule biogenesis. The smaller reduction in PC12 could be due to the endogenous expression of additional granin family members endowed with a granulogenic effect and which could act through PLD/PA-independent manner. Interestingly, this reduction in secretory granule number was also accompanied by an alteration in the shape of these organelles, very similarly to what was found in CgA-knockout chromaffin cells (52), indicating that PLD1 depletion partially phenocopies CgA deficiency regarding the impact on secretory granule biogenesis. These observations strongly suggest again that CgA and PLD1-generated PA cooperate to trigger the formation of secretory granules in neuroendocrine cells.

Finally, it must be pointed out that a recent study based on *in vitro* reconstitution assays and molecular modeling reported additional functions of specific species of PA during COPI vesicle fission (53). Indeed, PA generated by lysophosphatidic acid acyltransferase type gamma promotes the early stage of COPI vesicle fission whereas PA generated by phospholipase D type 2 promotes the late stage of fission. Intriguingly, PA with shorter fatty acid chains better supported the later function of PA, most likely by triggering the activity of BARS (53). It is of note that our lipidomic analysis indicates that these shorter forms of PA are scarce in Golgi or secretory granule membranes suggesting that only a tiny fraction of PA

could trigger the fission of budding vesicle, while larger proportion of PA is required for budding. A recent study revealed that PI4P in the cytosolic leaflet of the TGN membrane recruits cytosolic proteins such as GOLPH3 through its membrane curvature ability (54), suggesting that PA could also initiate this process by activating Golgi PIP-kinase to produce PI4P in the cytosolic leaflet.

Altogether, our data show that CgA binds to specific species of PA which in turn could act as lipid cofactors (55) at the TGN to induce membrane remodeling and curvature in order to initiate secretory granule budding, concomitantly or prior to the recruitment of cytosolic proteins such as GOLPH3 (54), arfaptins (56, 57), the acto-myosin 1b complex (58) or the membrane-associated myristoylated protein HID1 (59), but also small GTPase of the Arf family (60), all of which are also essential actors in this fundamental biological process necessary for regulated secretion. Further studies are now needed to evaluate the connection of CgA/PA interaction with the additional machinery involved in secretory granule biogenesis, in living neuroendocrine cells, and the potential implication of this interaction in diseases related to hormone secretion deregulation.

ACKNOWLEDGEMENTS

We thank Jérôme Leprince for fruitful discussion for PABD modelization. This work was supported by institutional funding from INSERM, University of Rouen-Normandie, IBiSA, IRIB, Région Normandie, the European Regional Development Funds (ERDF DO-IT2015 and ERDF – PACT-CBS programs), and grant from the Medical Research Foundation (FRM) (project number DEI20151234424) to MM-H, P-YR and NV. OC and CD-D were supported by fellowships from the Ministère de la Recherche et de l'Enseignement Supérieur. FL is co-supported by European Union and Région Normandie. LR was supported by fellowship from FRM. Lipidomic analyses were performed on the Bordeaux Metabolome Facility-MetaboHUB (ANR-11-INBS-0010). The authors declare that no competing interests exist.

AUTHOR CONTRIBUTIONS

OC, FL and LR: designed and performed most of the experiments, analyzed the data and contributed to writing of the paper. CD-D: performed and analyzed lipid overlay assays. QW: performed some immunofluorescence and electron microscopy experiments and associated quantifications. ET and TT: performed the experiments related to liposome flotation and

binding assays. LJ: managed cell line culture and secretion experiments. DC: contributed to CgA-GFP and CgAΔPABD-GFP cloning. AMH: performed electron microscopy experiments and associated quantifications. LF: performed the lipidome analysis using LC-MS/MS. OR, AH and P-YR: produced CgA coupled to Alexa Fluor 488 dye. DS and LG: performed super-resolution observations using STED nanoscope. YG: synthesized recombinant CgA. SA: designed AFM and ITC setup, and analyzed AFM and ITC data. NV: designed liposome flotation and binding assays, analyzed data from electron microscopy experiments, performed PA-binding domain prediction, and contributed to writing of the paper. YA: contributed to experiment design, data analysis and interpretation, and writing of the paper. MM-H: coordinated the study, designed, analyzed and interpreted data, and wrote the paper.

REFERENCES

1. Tanguy, E., Carmon, O., Wang, Q., Jeandel, L., Chasserot-Golaz, S., Montero-Hadjadje, M., and Vitale, N. (2016) Lipids implicated in the journey of a secretory granule: from biogenesis to fusion. *J. Neurochem.* **137**, 904–912

2. Holthuis, J. C. M. and Menon, A. K. (2014) Lipid landscapes and pipelines in membrane homeostasis. *Nature* **510**, 48–57

3. Surma, M. A., Klose, C., and Simons, K. (2012) Lipid-dependent protein sorting at the trans-Golgi network. *Biochim. Biophys. Acta - Mol. Cell Biol. Lipids* **1821**, 1059–1067

4. Dhanvantari, S., Arnaoutova, I., Snell, C. R., Steinbach, P. J., Hammond, K., Caputo, G. A., London, E., and Loh, Y. P. (2002) Carboxypeptidase E, a prohormone sorting receptor, is anchored to secretory granules via a C-terminal transmembrane insertion. *Biochemistry* **41**, 52–60

5. Gondré-Lewis, M. C., Petrache, H. I., Wassif, C. A., Harries, D., Parsegian, A., Porter, F. D., and Loh, Y. P. (2006) Abnormal sterols in cholesterol-deficiency diseases cause secretory granule malformation and decreased membrane curvature. *J. Cell Sci.* **119**, 1876–1885

6. Duran, J. M., Campelo, F., van Galen, J., Sachsenheimer, T., Sot, J., Egorov, M. V, Rentero, C., Enrich, C., Polishchuk, R. S., Goñi, F. M., Brügger, B., Wieland, F., and Malhotra, V. (2012) Sphingomyelin organization is required for vesicle biogenesis at the Golgi complex. *EMBO J.* **31**, 4535–4546

7. Makowski, S. L., Kuna, R. S., and Field, S. J. (2019) Induction of membrane curvature by proteins involved in Golgi trafficking. *Adv. Biol. Regul.* 100661

8. Montero-Hadjadje, M., Vaingankar, S., Elias, S., Tostivint, H., Mahata, S. K., and Anouar, Y. (2008) Chromogranins A and B and secretogranin II: Evolutionary and functional aspects. *Acta Physiol.* **192**, 309–324

9. Chanat, E. and Huttner, W. B. (1991) Milieu-induced, selective aggregation of regulated secretory proteins in the trans-Golgi network. *J. Cell Biol.* **115**, 1505–1519

10. Kim, T., Tao-Cheng, J. H., Eiden, L. E., and Loh, Y. P. (2001) Chromogranin A, an "on/off" switch controlling dense-core secretory granule biogenesis. *Cell* **106**, 499–509

11. Elias, S., Delestre, C., Courel, M., Anouar, Y., and Montero-Hadjadje, M. (2010) Chromogranin A as a crucial factor in the sorting of peptide hormones to secretory granules. *Cell. Mol. Neurobiol.* **30**, 1189–1195

12. Mahapatra, N. R., O'Connor, D. T., Vaingankar, S. M., Hikim, A. P. S., Mahata, M., Ray, S., Staite, E., Wu, H., Gu, Y., Dalton, N., Kennedy, B. P., Ziegler, M. G., Ross, J., and Mahata, S. K. (2005) Hypertension from targeted ablation of chromogranin A can be rescued by the human ortholog. *J. Clin. Invest.* **115**, 1942–1952

13. Bandyopadhyay, G. K. and Mahata, S. K. (2017) Chromogranin A Regulation of Obesity and Peripheral Insulin Sensitivity. *Front. Endocrinol. (Lausanne).* **8**, 20

14. Montero-Hadjadje, M., Elias, S., Chevalier, L., Benard, M., Tanguy, Y., Turquier, V., Galas, L., Yon, L., Malagon, M. M., Driouich, A., Gasman, S., and Anouar, Y. (2009) Chromogranin A promotes peptide hormone sorting to mobile granules in constitutively and regulated secreting cells. Role of conserved N- and C-terminal peptides. *J. Biol. Chem.* **284**, 12420–12431

15. Elias, S., Delestre, C., Ory, S., Marais, S., Courel, M., Vazquez-Martinez, R., Bernard, S., Coquet, L., Malagon, M. M., Driouich, A., Chan, P., Gasman, S., Anouar, Y., and Montero-Hadjadje, M. (2012) Chromogranin A induces the biogenesis of granules with calcium- and actin-dependent dynamics and exocytosis in constitutively secreting cells. *Endocrinology* **153**, 4444–4456

16. Kang, Y. K. and Yoo, S. H. (1997) Identification of the secretory vesicle membrane binding region of chromogranin A. *FEBS Lett.* **404**, 87–90

17. Abbineni, P. S., Bittner, M. A., Axelrod, D., and Holz, R. W. (2019) Chromogranin A, the major lumenal protein in chromaffin granules, controls fusion pore expansion. *J. Gen. Physiol.* **151**, 118–130

18. Blois, A., Holmsen, H., Martino, G., Corti, A., Metz-Boutigue, M. H., and Helle, K. B. (2006) Interactions of chromogranin A-derived vasostatins and monolayers of phosphatidylserine, phosphatidylcholine and phosphatidylethanolamine. *Regul. Pept.* **134**, 30–37

19. Dondossola, E., Gasparri, A., Bachi, A., Longhi, R., Metz-Boutigue, M.-H., Tota, B., Helle, K. B., Curnis, F., and Corti, A. (2010) Role of vasostatin-1 C-terminal region in fibroblast cell adhesion. *Cell. Mol. Life Sci.* **67**, 2107–2118

20. Sugawara, M., Resende, J. M., Moraes, C. M., Marquette, A., Chich, J.-F., Metz-Boutigue, M.-H., and Bechinger, B. (2010) Membrane structure and interactions of human catestatin by multidimensional solution and solid-state NMR spectroscopy. *FASEB J.* **24**, 1737–1746

21. Kassas, N., Tanguy, E., Thahouly, T., Fouillen, L., Heintz, D., Chasserot-Golaz, S., Bader, M.-F., Grant, N. J., and Vitale, N. (2017) Comparative Characterization of Phosphatidic Acid Sensors and Their Localization during Frustrated Phagocytosis. *J. Biol. Chem.* **292**, 4266–4279

22. Ammar, M.-R., Humeau, Y., Hanauer, A., Nieswandt, B., Bader, M.-F., and Vitale, N. (2013) The Coffin-Lowry Syndrome-Associated Protein RSK2 Regulates Neurite Outgrowth through Phosphorylation of Phospholipase D1 (PLD1) and Synthesis of Phosphatidic Acid. *J. Neurosci.* **33**, 19470–19479

23. Ammar, M. R., Thahouly, T., Hanauer, A., Stegner, D., Nieswandt, B., and Vitale, N. (2015) PLD1 participates in BDNF-induced signalling in cortical neurons. *Sci. Rep.* **5**, 14778

24. Chevalier, A., Massif, C., Renard, P.-Y., and Romieu, A. (2013) Bioconjugatable Azo-Based Dark-Quencher Dyes: Synthesis and Application to Protease-Activatable Far-Red Fluorescent Probes. *Chemistry* **19**, 1686–1699

25. Montero-Hadjadje, M., Vaudry, H., Turquier, V., Leprince, J., Do Rego, J.-L., Yon, L., Gallo-Payet, N., Plouin, P.-F., and Anouar, Y. (2002) Localization and characterization of evolutionarily conserved chromogranin A-derived peptides in the rat and human

pituitary and adrenal glands. *Cell Tissue Res.* **310**, 223–236

26. Anouar, Y., Desmoucelles, C., Yon, L., Leprince, J., Breault, L., Gallo-Payet, N., and Vaudry, H. (1998) Identification of a Novel Secretogranin II-Derived Peptide (SgII $_{187–252}$) in Adult and Fetal Human Adrenal Glands Using Antibodies Raised against the Human Recombinant Peptide. *J. Clin. Endocrinol. Metab.* **83**, 2944–2951

27. Graham, J. M. (2001) Isolation of Golgi Membranes from Tissues and Cells by Differential and Density Gradient Centrifugation. *Curr. Protoc. Cell Biol.* **10**, 3.9.1-3.9.24

28. Bligh, E. G. and Dyer, W. J. (1959) A rapid method of total lipid extraction and purification. *Can. J. Biochem. Physiol.* **37**, 911–917

29. Shui, G., Guan, X. L., Low, C. P., Chua, G. H., Goh, J. S. Y., Yang, H., and Wenk, M. R. (2010) Toward one step analysis of cellular lipidomes using liquid chromatography coupled with mass spectrometry: application to Saccharomyces cerevisiae and Schizosaccharomyces pombe lipidomics. *Mol. Biosyst.* **6**, 1008

30. Bénard, M., Schapman, D., Lebon, A., Monterroso, B., Bellenger, M., Le Foll, F., Pasquier, J., Vaudry, H., Vaudry, D., and Galas, L. (2015) Structural and functional analysis of tunneling nanotubes (TnTs) using gCW STED and gconfocal approaches. *Biol. cell* **107**, 419–425

31. Galas, L., Gallavardin, T., Bénard, M., Lehner, A., Schapman, D., Lebon, A., Komuro, H., Lerouge, P., Leleu, S., and Franck, X. (2018) “Probe, Sample, and Instrument (PSI)”: The Hat-Trick for Fluorescence Live Cell Imaging. *Chemosensors* **6**, 40

32. Huston, E., Gall, I., Houslay, T. M., and Houslay, M. D. (2006) Helix-1 of the cAMP-specific phosphodiesterase PDE4A1 regulates its phospholipase-D-dependent redistribution in response to release of Ca2+. *J. Cell Sci.* **119**, 3799–3810

33. Gautier, R., Douguet, D., Antonny, B., and Drin, G. (2008) HELIQUEST: a web server to screen sequences with specific alpha-helical properties. *Bioinformatics* **24**, 2101–2102

34. Tanguy, E., Kassas, N., and Vitale, N. (2018) Protein–Phospholipid Interaction Motifs: A Focus on Phosphatidic Acid. *Biomolecules* **8**, 20

35. Pierce, M. M., Raman, C. S., and Nall, B. T. (1999) Isothermal titration calorimetry of

protein-protein interactions. *Methods* **19**, 213–221

36. Miao, R., Lung, S.-C., Li, X., Li, X. D., and Chye, M.-L. (2019) Thermodynamic insights into an interaction between acyl-coa–binding protein2 and lysophospholipase2 in *Arabidopsis*. *J. Biol. Chem.* **294**, 6214–6226

37. Freyberg, Z., Siddhanta, A., and Shields, D. (2003) "Slip, sliding away": phospholipase D and the Golgi apparatus. *Trends Cell Biol.* **13**, 540–546

38. Freyberg, Z., Sweeney, D., Siddhanta, A., Bourgoin, S., Frohman, M., and Shields, D. (2001) Intracellular Localization of Phospholipase D1 in Mammalian Cells. *Mol. Biol. Cell* **12**, 943–955

39. Gondré-Lewis, M. C., Park, J. J., and Loh, Y. P. (2012) Cellular mechanisms for the biogenesis and transport of synaptic and dense-core vesicles. *Int. Rev. Cell Mol. Biol.* **299**, 27–115

40. Siddhanta, A. and Shields, D. (1998) Secretory vesicle budding from the trans-Golgi network is mediated by phosphatidic acid levels. *J. Biol. Chem.* **273**, 17995–17998

41. Cullis, P. R., Hope, M. J., Bally, M. B., Madden, T. D., Mayer, L. D., and Fenske, D. B. (1997) Influence of pH gradients on the transbilayer transport of drugs, lipids, peptides and metal ions into large unilamellar vesicles. *Biochim. Biophys. Acta* **1331**, 187–211

42. Pomorski, T. G. and Menon, A. K. (2016) Lipid somersaults: Uncovering the mechanisms of protein-mediated lipid flipping. *Prog. Lipid Res.* **64**, 69–84

43. Braks, J. A. M. and Martens, G. J. M. (1994) 7B2 is a neuroendocrine chaperone that transiently interacts with prohormone convertase PC2 in the secretory pathway. *Cell* **78**, 263–273

44. Aunis, D. and Metz-Boutigue, M. H. (2001) Chromogranines: De la découverte à la fonction. *Medecine/Sciences* **17**, 418–427

45. Taupenot, L., Harper, K. L., and O'Connor, D. T. (2003) The Chromogranin–Secretogranin Family. *N. Engl. J. Med.* **348**, 1134–1149

46. Potocký, M., Pleskot, R., Pejchar, P., Vitale, N., Kost, B., and Žárský, V. (2014) Live-cell imaging of phosphatidic acid dynamics in pollen tubes visualized by Spo20p-

derived biosensor. *New Phytol.* **203**, 483–494

47. Kooijman, E. E., Chupin, V., de Kruijff, B., and Burger, K. N. J. (2003) Modulation of membrane curvature by phosphatidic acid and lysophosphatidic acid. *Traffic* **4**, 162–174

48. Sahu, B. S., Obbineni, J. M., Sahu, G., Allu, P. K. R., Subramanian, L., Sonawane, P. J., Singh, P. K., Sasi, B. K., Senapati, S., Maji, S. K., Bera, A. K., Gomathi, B. S., Mullasari, A. S., and Mahapatra, N. R. (2012) Functional Genetic Variants of the Catecholamine-Release-Inhibitory Peptide Catestatin in an Indian Population. *J. Biol. Chem.* **287**, 43840–43852

49. Kiranmayi, M., Chirasani, V. R., Allu, P. K. R., Subramanian, L., Martelli, E. E., Sahu, B. S., Vishnuprabu, D., Kumaragurubaran, R., Sharma, S., Bodhini, D., Dixit, M., Munirajan, A. K., Khullar, M., Radha, V., Mohan, V., Mullasari, A. S., Naga Prasad, S. V., Senapati, S., and Mahapatra, N. R. (2016) Catestatin Gly364Ser Variant Alters Systemic Blood Pressure and the Risk for Hypertension in Human Populations via Endothelial Nitric Oxide Pathway. *Hypertension* **68**, 334–347

50. Riebeling, C., Morris, A. J., and Shields, D. (2009) Phospholipase D in the Golgi apparatus. *Biochim. Biophys. Acta* **1791**, 876–880

51. Vitale, N., Caumont, A. S., Chasserot-Golaz, S., Du, G., Wu, S., Sciorra, V. A., Morris, A. J., Frohman, M. A., and Bader, M. F. (2001) Phospholipase D1: a key factor for the exocytotic machinery in neuroendocrine cells. *EMBO J.* **20**, 2424–2434

52. Pasqua, T., Mahata, S., Bandyopadhyay, G. K., Biswas, A., Perkins, G. A., Sinha-Hikim, A. P., Goldstein, D. S., Eiden, L. E., and Mahata, S. K. (2016) Impact of Chromogranin A deficiency on catecholamine storage, catecholamine granule morphology and chromaffin cell energy metabolism in vivo. *Cell Tissue Res.* **363**, 693–712

53. Park, S. Y., Yang, J. S., Li, Z., Deng, P., Zhu, X., Young, D., Ericsson, M., Andringa, R. L. H., Minnaard, A. J., Zhu, C., Sun, F., Moody, D. B., Morris, A. J., Fan, J., and Hsu, V. W. (2019) The late stage of COPI vesicle fission requires shorter forms of phosphatidic acid and diacylglycerol. *Nat. Commun.* **10**, 1–14

54. Rahajeng, J., Kuna, R. S., Makowski, S. L., Tran, T. T. T., Buschman, M. D., Li, S., Cheng, N., Ng, M. M., and Field, S. J. (2019) Efficient Golgi Forward Trafficking

Requires GOLPH3-Driven, PI4P-Dependent Membrane Curvature. *Dev. Cell* **50**, 573–585

55. Zhukovsky, M. A., Filograna, A., Luini, A., Corda, D., and Valente, C. (2019) Protein Amphipathic Helix Insertion : A Mechanism to Induce Membrane Fission. *Front. Cell Dev. Biol.* **7**, 1–29

56. Cruz-Garcia, D., Ortega-Bellido, M., Scarpa, M., Villeneuve, J., Jovic, M., Porzner, M., Balla, T., Seufferlein, T., and Malhotra, V. (2013) Recruitment of arfaptins to the trans-Golgi network by PI(4)P and their involvement in cargo export. *EMBO J.* **32**, 1717–1729

57. Gehart, H., Goginashvili, A., Beck, R., Morvan, J., Erbs, E., Formentini, I., De Matteis, M. A., Schwab, Y., Wieland, F. T., and Ricci, R. (2012) The BAR Domain Protein Arfaptin-1 Controls Secretory Granule Biogenesis at the trans-Golgi Network. *Dev. Cell* **23**, 756–768

58. Delestre-Delacour, C., Carmon, O., Laguerre, F., Estay-Ahumada, C., Courel, M., Elias, S., Jeandel, L., Rayo, M. V., Peinado, J. R., Sengmanivong, L., Gasman, S., Coudrier, E., Anouar, Y., and Montero-Hadjadje, M. (2017) Myosin 1b and F-actin are involved in the control of secretory granule biogenesis. *Sci. Rep.* **7**,5172

59. Hummer, B. H., de Leeuw, N. F., Burns, C., Chen, L., Joens, M. S., Hosford, B., Fitzpatrick, J. A. J., and Asensio, C. S. (2017) HID-1 controls formation of large dense core vesicles by influencing cargo sorting and trans-Golgi network acidification. *Mol. Biol. Cell* **28**, 3870–3880

60. Vitale, N., Chasserot-Golaz, S., Bailly, Y., Morinaga, N., Frohman, M. A., and Bader, M. F. (2002) Calcium-regulated exocytosis of dense-core vesicles requires the activation of ADP-ribosylation factor (ARF)6 by ARF nucleotide binding site opener at the plasma membrane. *J. Cell Biol.* **159**, 79–89

FIGURE LEGENDS

Figure 1. CgA interacts with PA through a putative PABD and Golgi PA is involved in CgA secretory granule biogenesis.

A Protein–lipid overlay assay in the presence of recombinant CgA (500 ng/ml) using commercial membrane strips where 100 pmol/spot of the following lipids are adsorbed: triglycerides, diacylglycerol (DAG), phosphatidic acid (PA), phosphatidylserine (PS), phosphatidylethanolamine (PE), phosphatidylcholine (PC), phosphatidylglycerol (PG), cardiolipin, phosphatidylinositol (PI), phosphatidylinositol 4-phosphate (PI(4)P), phosphatidylinositol 4,5-bisphosphate ($PI(4,5)P_2$), phosphatidylinositol 3,4,5-trisphosphate ($PI(3,4,5)P_3$), cholesterol, sphingomyelin, or 3-sulfogalactosylceramide (sulfatide). After the overlay, the membrane was immunostained for CgA using the anti-WE-14 antibody, and revealed using a chemiluminescence kit. Plotted are means of CgA binding intensity expressed as percentage normalized to control (blank) ± s.e.m. (n=3). ***$P < 0.001$, Anova one-way analysis of variance test with Bonferroni's comparison test.

B Involvement of Golgi PA in the formation of CgA-containing secretory granules in PC12 cells. Cells expressing wild-type PDE4A1 coupled with GFP (PDE4A1(PABD)) or PABD-mutated PDE4A1 coupled with GFP (PDE4A1(PABD Mut)) are surrounded by a dashed line. Cells were immunolabelled with anti-CgA antibody and their fluorescence was examined using confocal microscopy. Representative confocal microscopy sections throughout the cells are shown. Values for the intensity of CgA staining and the number of granules per cell are plotted as the means ± S.D. (n=2; 40 cells per condition). **$P < 0.01$, Mann-Whitney test. The scale bar represents 20 μm. Western blots show expression of CgA and α-tubulin as loading control.

C Human CgA (hCgA) sequence showing a region of 18 amino acids (364-381), encompassing a positive charge cluster and hydrophobic residues that could adopt an α-helical conformation, delimited by arrows, suggesting its function as PA-binding domain (PABD).

D PA binding profile of the putative human CgA-PABD. Amphipathic α-helix projection of the core 18 amino acids of the PABD of CgA obtained with Heliquest software. Arrow indicates hydrophobic moment. Red N and C indicate the beginning and the end of PABD amino acid sequence.

E Model of the putative human CgA-PABD. Ribbon corresponds to the α-helix. The structure was determined using MacPyMOL (v1.74).

F Characterization of the PA binding capacity of human CgA through the putative PABD. Semi-quantitative fluorescent liposome assays with fluorescent liposomes (5% PE-NBD, 95% DOPC) or PA-containing fluorescent liposomes (5% PE-NBD, 85% DOPC, 10% PA mix) and GST-CgA-PABD constructs linked to GSH-sepharose beads. The binding of liposomes with CgA-PABD constructs was monitored by fluorimetry. Results are presented as means ± S.D. (triplicate measurements; n=3).

Figure 2. Same predominant PA species are found in Golgi and secretory granule membranes from COS7-WT, COS7-CgA and PC12 cells.

A The level of distinct PA species was measured in fractions of secretory granule (SG) and Golgi membranes from COS7-CgA cells by duplicate UPLC/MS/MS analysis of two samples (each containing 200 µg of protein) from each fraction. The acyl chain composition of each species is shown on the x axis. The y axis shows the abundance of each species as a percentage of total PA in the sample.

B PA levels were measured in fractions of Golgi membranes from COS7-WT or COS7-CgA cells by duplicate UPLC/MS/MS analysis of two samples (each containing 200 µg of protein) from each fraction. The acyl chain composition of each species is shown on the x axis. The y axis shows the abundance of each species as a percentage of total PA in the sample.

C PA levels were measured in secretory granule-containing fractions from PC12 or COS7-CgA cells by duplicate UPLC/MS/MS analysis of two samples (each containing 200 µg of protein) from each fraction. The acyl chain composition of each species is shown on the x axis. The y axis shows the abundance of each species as a percentage of total PA in the sample.

Figure 3. CgA interacts with PA species identified in Golgi and secretory granule membranes and provokes membrane deformation of PA-enriched GUVs.

A Schematic representation of the liposome flotation assay approach used to study the interaction of CgA from COS7-CgA cell extracts with PA species.

B Detection of CgA in the different fractions (Top (T), Medium (M), Bottom (B)) obtained from liposome assays. COS7-CgA cell extracts were incubated with liposomes containing 5% PE-NBD, 85% of DOPC, and 10% of the indicated phosphatidylcholine (PC), phosphatidylserine (PS), phosphatidylinositol-4,5-bisphosphate (PIP2), a commercial

phosphatidic acid mix (PA) or distinct species of PA (PA(36:0), PA(36:1) or PA(40:6)). Thirty µg of protein from each fraction were run on SDS-PAGE and immunoblotted with the WE-14 antibody.

C Formation of fluorescent PA-containing GUVs by PVA-assisted swelling. Stable fluorescent GUVs (95% DOPC, 4% PA(36:1) and 1% PE-NBD) were generated and observed by live confocal microscopy during 1 min. Representative confocal microscopy sections throughout the GUVs are shown. The scale bar represents 30 µm.

D Effect of CgA on fluorescent PA-containing GUVs. Fluorescent GUVs (95% DOPC, 4% PA(36:1) or PA(40:6) and 1% PE-NBD) were incubated with 2 µM CgA. Deformation of GUV membrane (arrows) was observed by live confocal microscopy during 1 min. Representative confocal microscopy sections throughout the GUVs are shown. The scale bar represents 30 µm.

E Quantification of generated vesicles following membrane deformation of PA-containing GUVs. GUVs (95% DOPC, 4% PA(36:1), 1% PE-NBD) were incubated with 2, 4 and 6 µM CgA (n=3; 35 videos per condition). ***$P < 0.001$, Mann-Whitney test. Means ± s.e.m. are plotted.

F Distribution of CgA-Alexa488 on PA-containing GUVs. GUVs (96% DOPC, 4% PA(36:1)) were incubated with 2 µM CgA-Alexa488. Staining and budding (arrows) of GUV membrane was observed by live confocal microscopy during 1 min. Representative confocal microscopy sections throughout the GUVs are shown. The scale bar represents 20 µm.

Figure 4. ITC analysis reveals that PA favors membrane incorporation of CgA.

A DOPC SUVs and CgA binding measured by titrating 5 µM CgA in the chamber with 10 mM vesicle suspension in the syringe. Top panel, raw heating power over time obtained with DOPC SUV injection in water; bottom panel, raw heating power over time obtained with DOPC SUV injection in CgA solution.

B DOPC/PA(36:1) SUVs and CgA binding measured by titrating 5 µM CgA in the chamber with 10 mM vesicle suspension in the syringe. Top panel, raw heating power over time obtained with DOPC/PA(36:1) SUV injection in water; bottom panel, raw heating power over time obtained with DOPC/PA(36:1) SUV injection in CgA solution.

C Fit curves of the integrated energy values obtained from A and B traces in bottom panels using A and B traces in top panels as blank, respectively. Experiments were carried out at 10°C, and each value is the mean of three independent titrations.

Figure 5. CgA induces the remodeling of PA-enriched membrane bilayers.

A Atomic force microscopy topographical images of mica supported bilayer surfaces from DOPC GUVs, incubated without or with 0.6 and 1.2 µM CgA, during 15 min (T1) and 75 min (T2). The scale bar represents 2 µm. The scheme corresponds to a topographical profile through an aggregate (enlarged view) showing a difference of height of 6 nm with the continuous phase.

B Atomic force microscopy topographical images of mica supported bilayer surfaces from DOPC/PA(36:1) (9:1, mol ratio) GUVs, incubated without or with 0.6 and 1.2 µM CgA, during 15 min (T1) and 75 min (T2). Arrow heads indicate aggregates that appeared at T1 and are maintained at T2; arrows indicate aggregates that appeared between T1 and T2. The scale bar represents 2 µm. The scheme corresponds to topographical profiles through aggregates (enlarged views) showing a difference of height of 6 nm (a) and 17 nm (b) with the continuous phase.

Figure 6. Number, surface and height of CgA-induced domains depend on PA enrichment of membrane bilayers.

A Scatter plot showing the number, area and height of domains obtained after incubation of supported bilayer surfaces from DOPC GUVs with 1.2 µM CgA during 75 min. Insert corresponds to enlarged view of the delimited zone emphasizing domains with height below 4 nm and area below 6,000 nm^2 (within blue surrounded zone). Analysis of domains was performed on 15 images and domains detected on an image are of the same color.

B Scatter plot showing the number, area and height of domains obtained after incubation of supported bilayer surfaces from DOPC/PA(36:1) (9:1, mol ratio) GUVs with 1.2 µM CgA during 75 min. Insert corresponds to enlarged view of the delimited zone emphasizing domains with height below 4 nm and area below 6,000 nm^2 (within blue surrounded zone). Analysis of domains was performed on 11 images and domains detected on an image are of the same color.

Figure 7. CgA PABD is required for secretory granule biogenesis.

A COS-7 cells transfected with plasmids encoding full-length CgA-GFP or CgA PABD-mutated form (CgAΔPABD)-GFP were examined for GFP fluorescence and GM130 immunoreactivity using confocal microscopy. Representative confocal microscopy sections throughout the cells are shown and were used to quantify automatically the granules with a diameter > 200 nm. Values for the number of granules/cell are plotted as the means ± s.e.m. (n=3; 65 cells per condition). ***$P < 0.001$, Mann-Whitney test. The scale bar represents 20 μm. Western blots show expression of CgA-GFP or CgAΔPABD-GFP fusion proteins and α-tubulin as loading control.

B AtT20 cells transfected with plasmids encoding full-length CgA-GFP or CgA PABD-mutated form (CgAΔPABD)-GFP were examined for GFP fluorescence and GM130 immunoreactivity using confocal microscopy. Representative confocal microscopy sections throughout the cells are shown and were used to quantify automatically the granules with a diameter > 200 nm. Values for the number of granules/cell are plotted as the means ± s.e.m. (n=3; 70 cells per condition). ***$P < 0.001$, Mann-Whitney test. The scale bar represents 20 μm. Western blots show expression of CgA-GFP or CgAΔPABD-GFP fusion proteins and α-tubulin as loading control.

C Golgi area of COS-7 cells transfected with plasmids encoding full-length CgA-GFP or CgA PABD-mutated form (CgAΔPABD)-GFP was examined for GFP fluorescence using *g*CW STED. Representative sections are shown after deconvolution. The scale bar represents 1 μm.

D Golgi area of AtT20 cells transfected with plasmids encoding full-length CgA-GFP or CgA PABD-mutated form (CgAΔPABD)-GFP was examined for GFP fluorescence using *g*CW STED. Representative sections are shown after deconvolution. The scale bar represents 1 μm.

Figure 8. Inhibition of PLD-mediated PA synthesis alters secretory granule biogenesis.

A COS7-CgA cells were treated or not with 75 nM FIPI for 6 h, fixed and immunolabelled with anti-GM130 and anti-CgA antibodies. Representative confocal microscopy sections throughout the cells are shown. The scale bar represents 20 μm. Values for the number of CgA secretory granules are plotted as the means ± s.e.m. (n=3; 60 cells per condition).

1159 ***$P < 0.001$, Mann-Whitney test. Western blots show expression of CgA and α-tubulin as
1160 loading control.

1161 B PC12 cells were treated or not with 75 nM FIPI for 6 h, fixed and immunolabelled with
1162 anti-GM130 and anti-CgA antibodies. Representative confocal microscopy sections
1163 throughout the cells are shown. The scale bar represents 10 µm. Values for the number of
1164 CgA secretory granules are plotted as the means ± s.e.m. (n=3; 60 cells per condition).
1165 Mann-Whitney test. Western blots show expression of CgA, CgB and SgII proteins, and α-
1166 tubulin as loading control.

1167 C Electron microscopy analysis of chromaffin cells from WT (control) and *Pld1*$^{-/-}$ mice.
1168 White arrows indicate representative secretory granules. The scale bars represent 2 µm.

1169 D Quantification of the number of secretory granules (SG) shown in panel (A) (n=6 mice per
1170 condition; 50 cells per mouse adrenal medulla). *$P < 0.05$, Mann-Whitney test.
1171 Means ± s.e.m. are plotted.

1172 E Quantification of the dense core diameter of secretory granules (SG) shown in panel (A)
1173 (n=6 mice per condition; 950 granules). *$P < 0.05$, Mann-Whitney test. Means ± s.e.m. are
1174 plotted.

Table 1.

Thermodynamic parameters for CgA binding on DOPC and DOPC/PA(36:1) SUVs. The values are plotted in Fig. 4C.

	DOPC		DOPC / PA(36 :1)	
	exothermic	endothermic	exothermic	endothermic
Kd (M)	$1.5\ 10^{-4} \pm 0.5\ 10^{-4}$	$2\ 10^{-5} \pm 1\ 10^{-5}$	$1.16\ 10^{-3} \pm 0.03\ 10^{-3}$	$3\ 10^{-4} \pm 0.1\ 10^{-4}$
n	259 ± 30	460 ± 40	199 ± 5	355 ± 5
ΔH (kJ/mol)	-1.82 ± 0.09	0.640 ± 0.06	-12.9 ± 0.3	7.65 ± 0.15
ΔS (J/mol.K)	67.3 ± 3.2	93.4 ± 4.8	10.6 ± 1.3	94.5 ± 0.8

Experiments were carried out at 10°C, and each value is the mean ± standard deviation from the fitted data of three independent experiments. Kd, dissociation constant; n, number of binding sites; ΔH, enthalpy change; ΔS, entropy change.

Figure 1

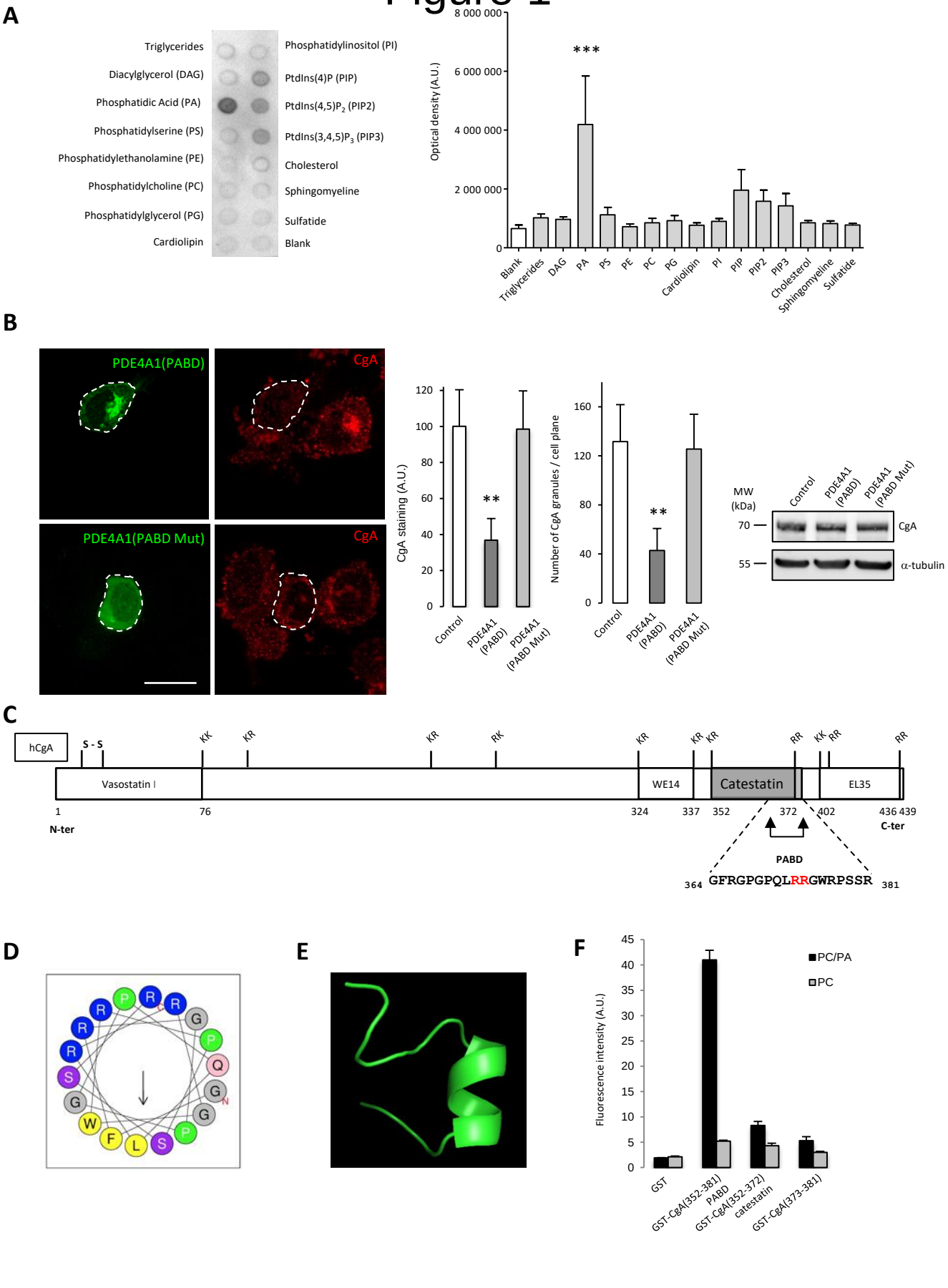

Figure 1

Figure 2

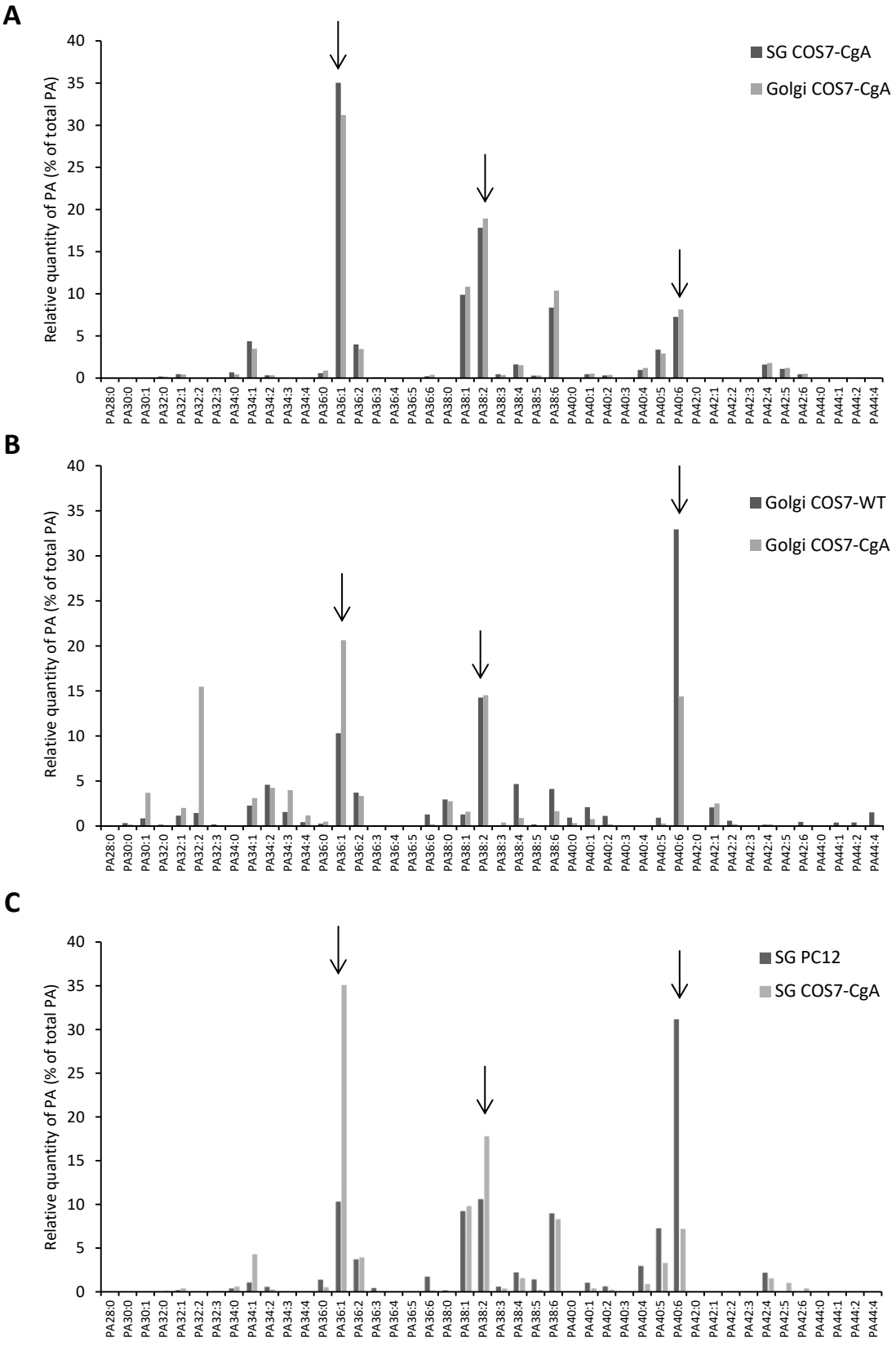

Figure 2

Figure 3

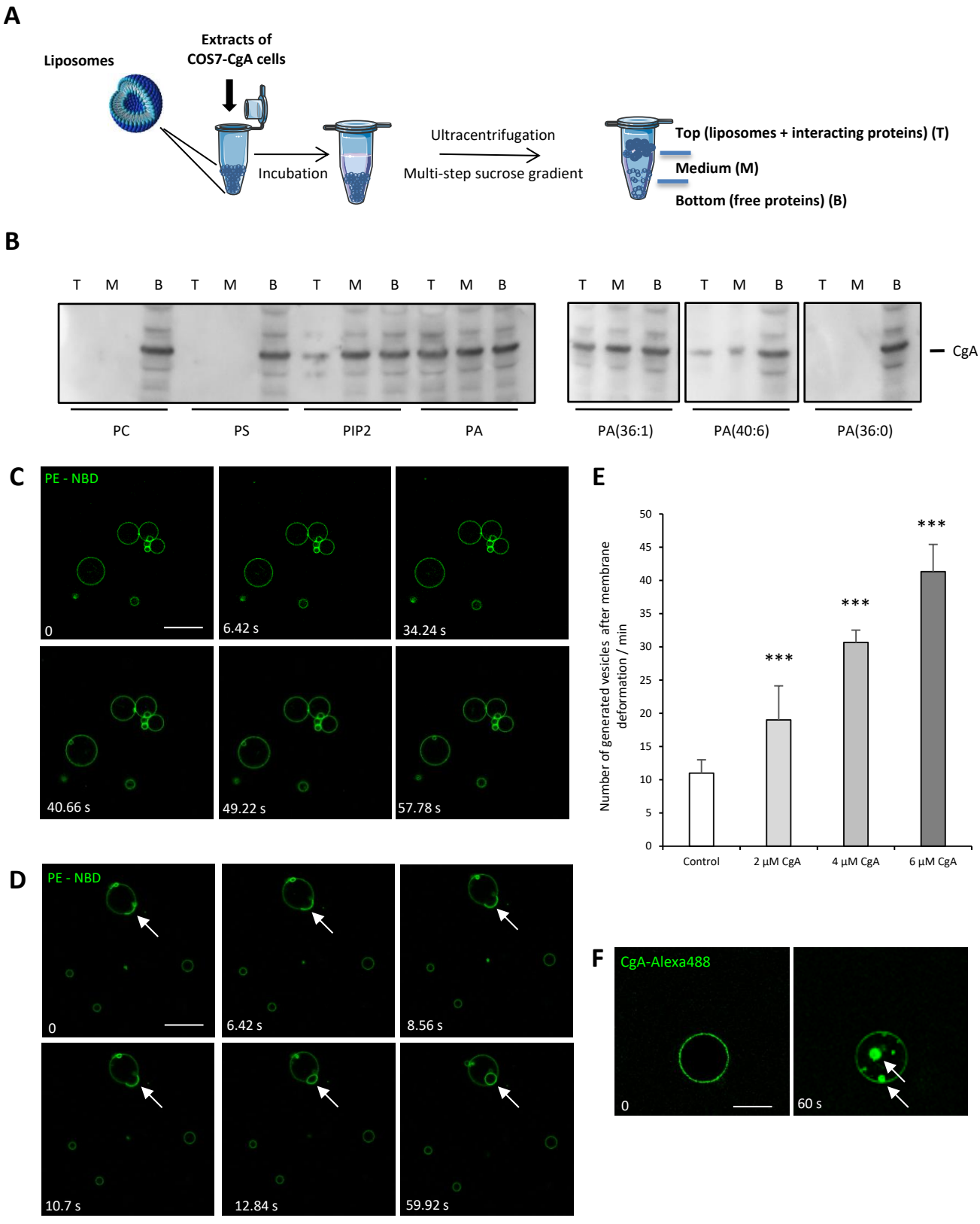

Figure 3

Figure 4

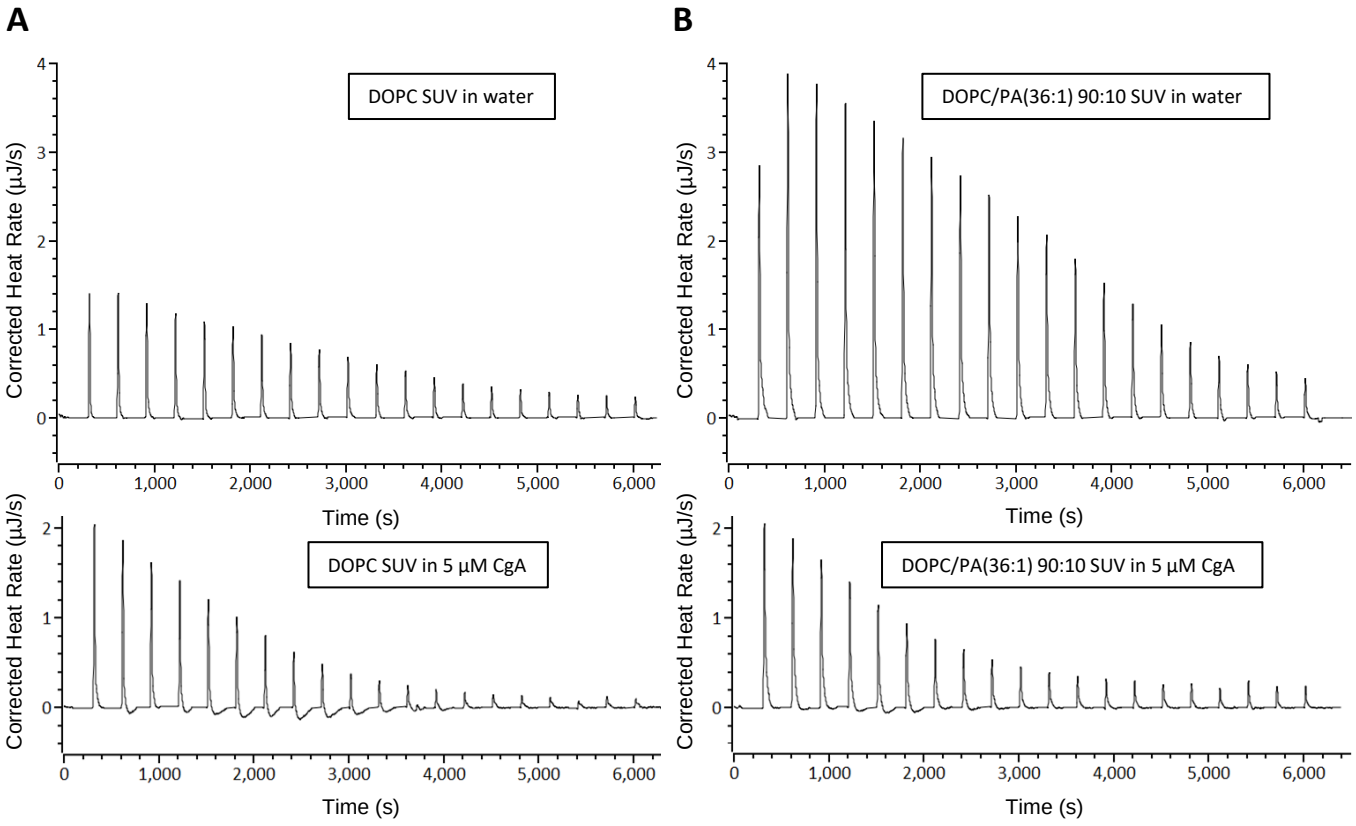

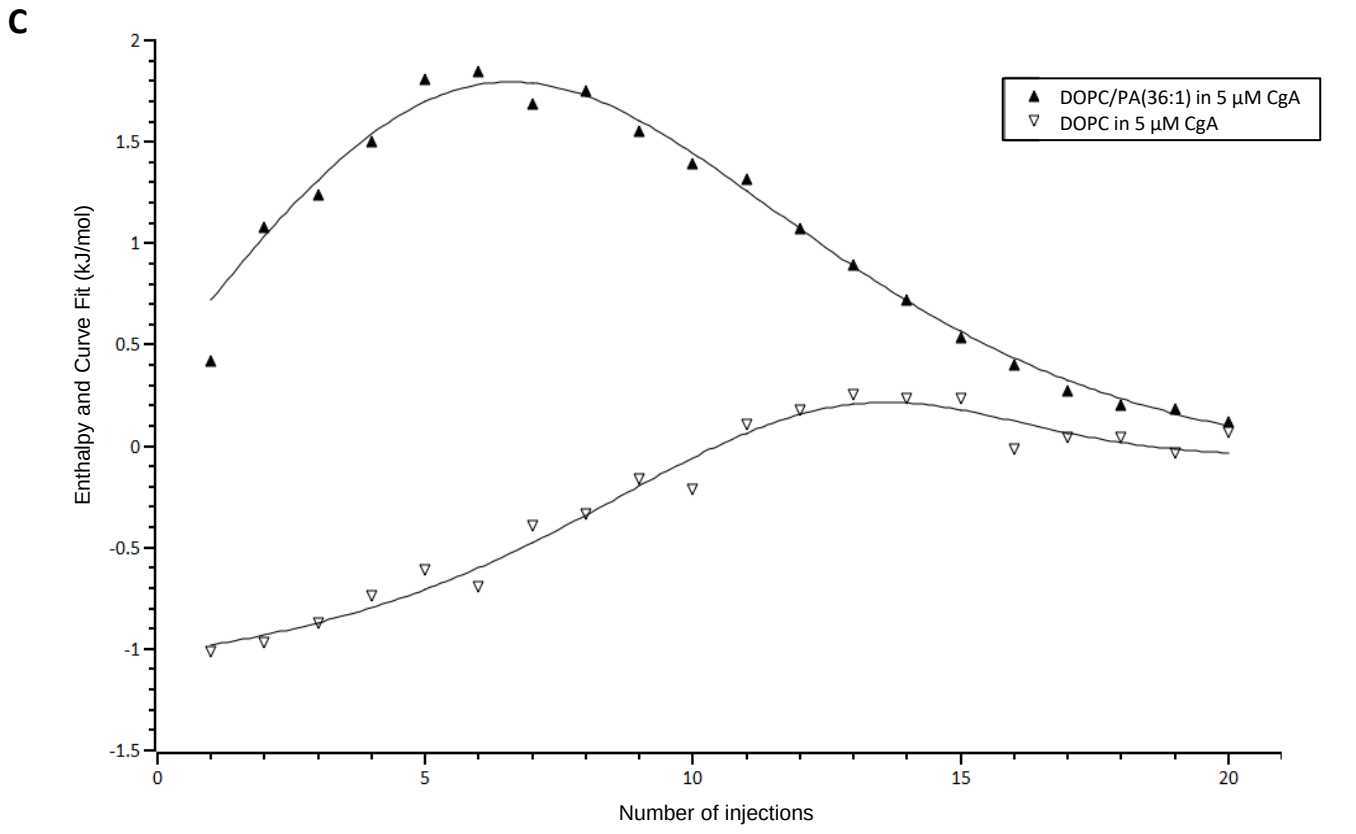

Figure 4

Figure 5

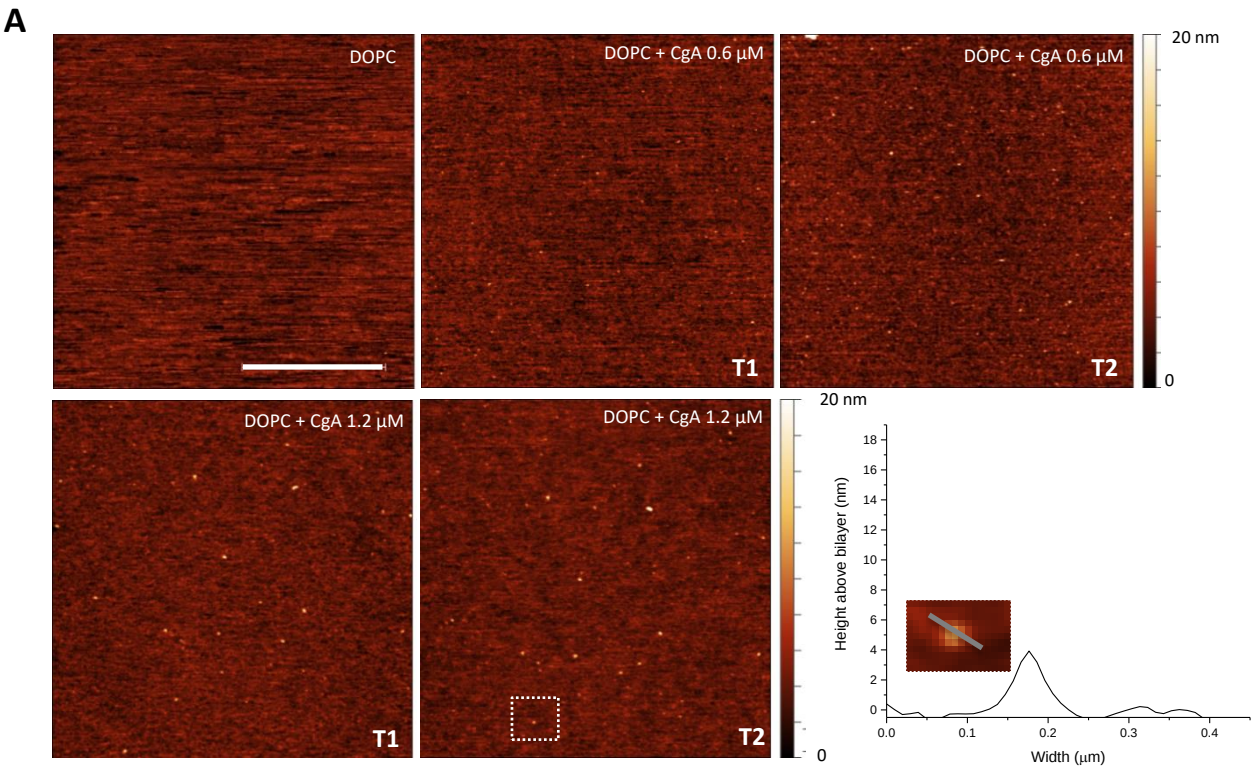

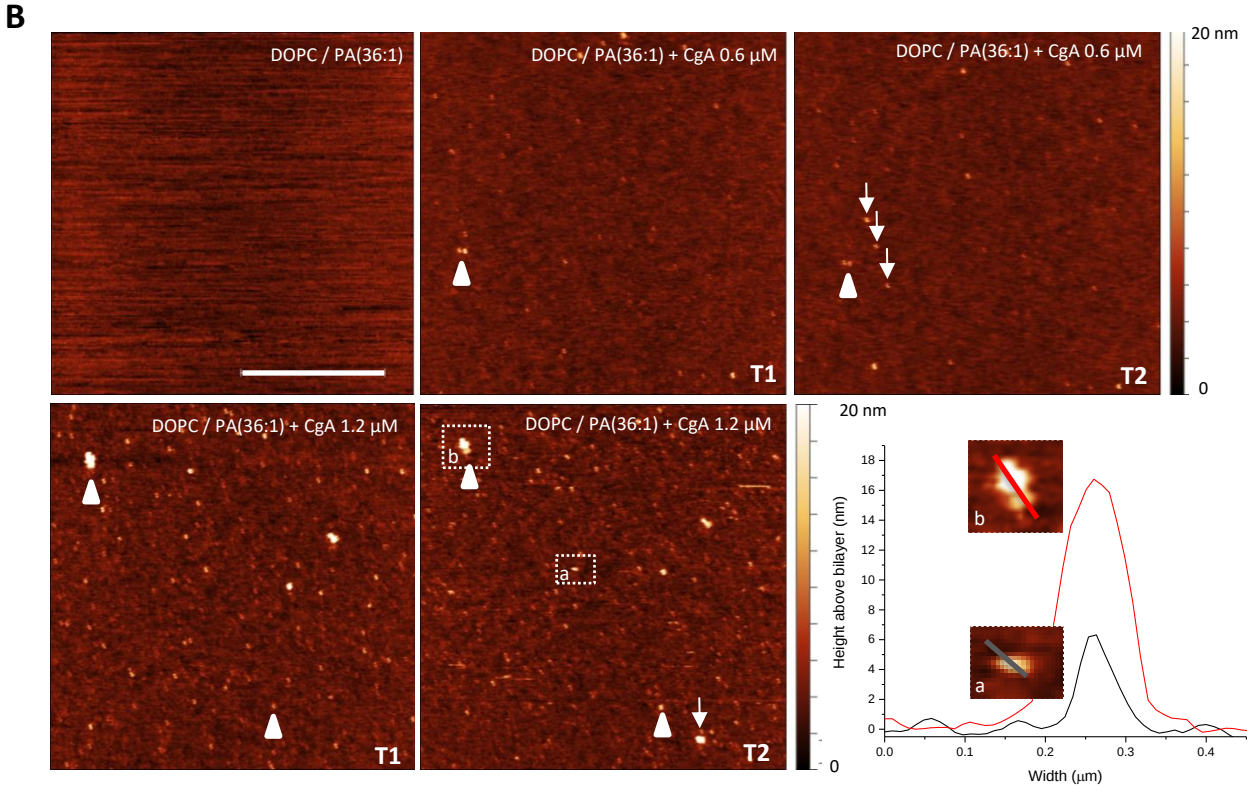

Figure 5

Figure 6

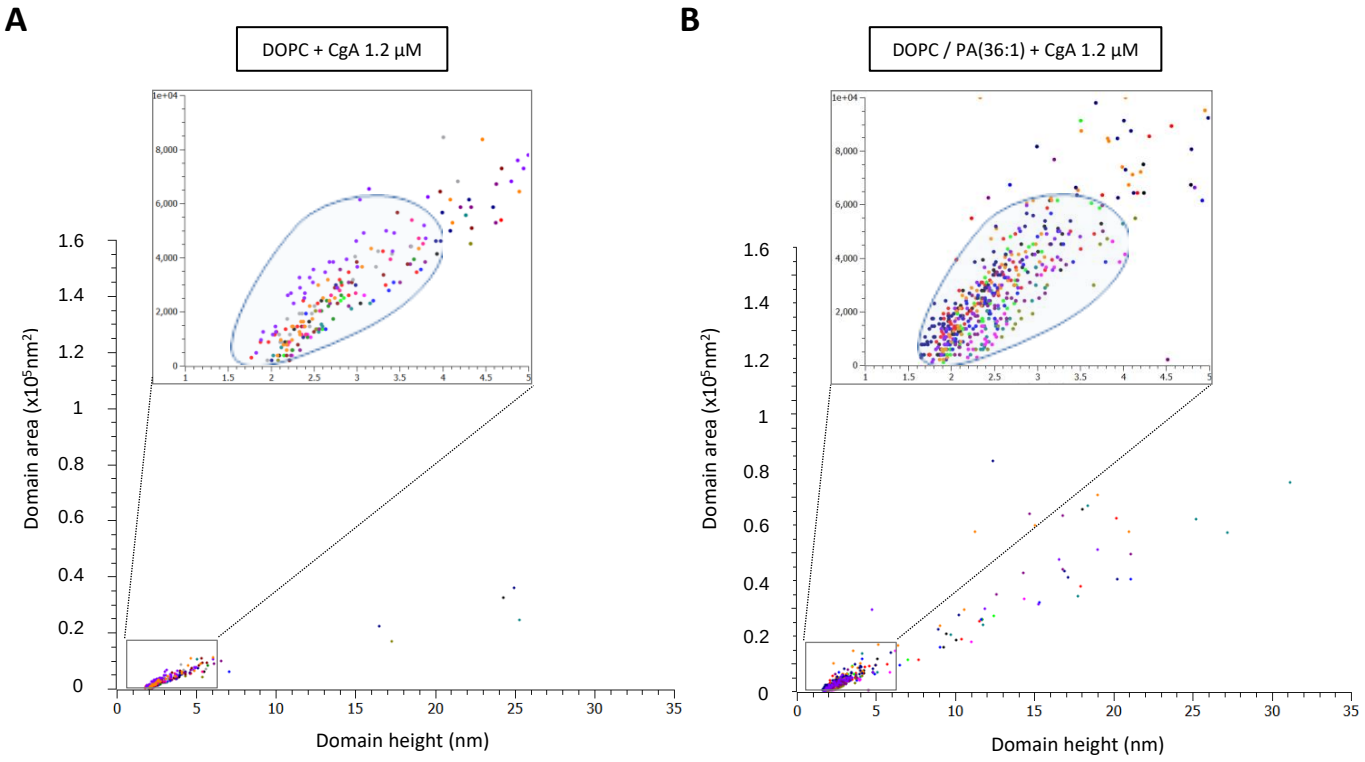

Figure 6

Figure 7

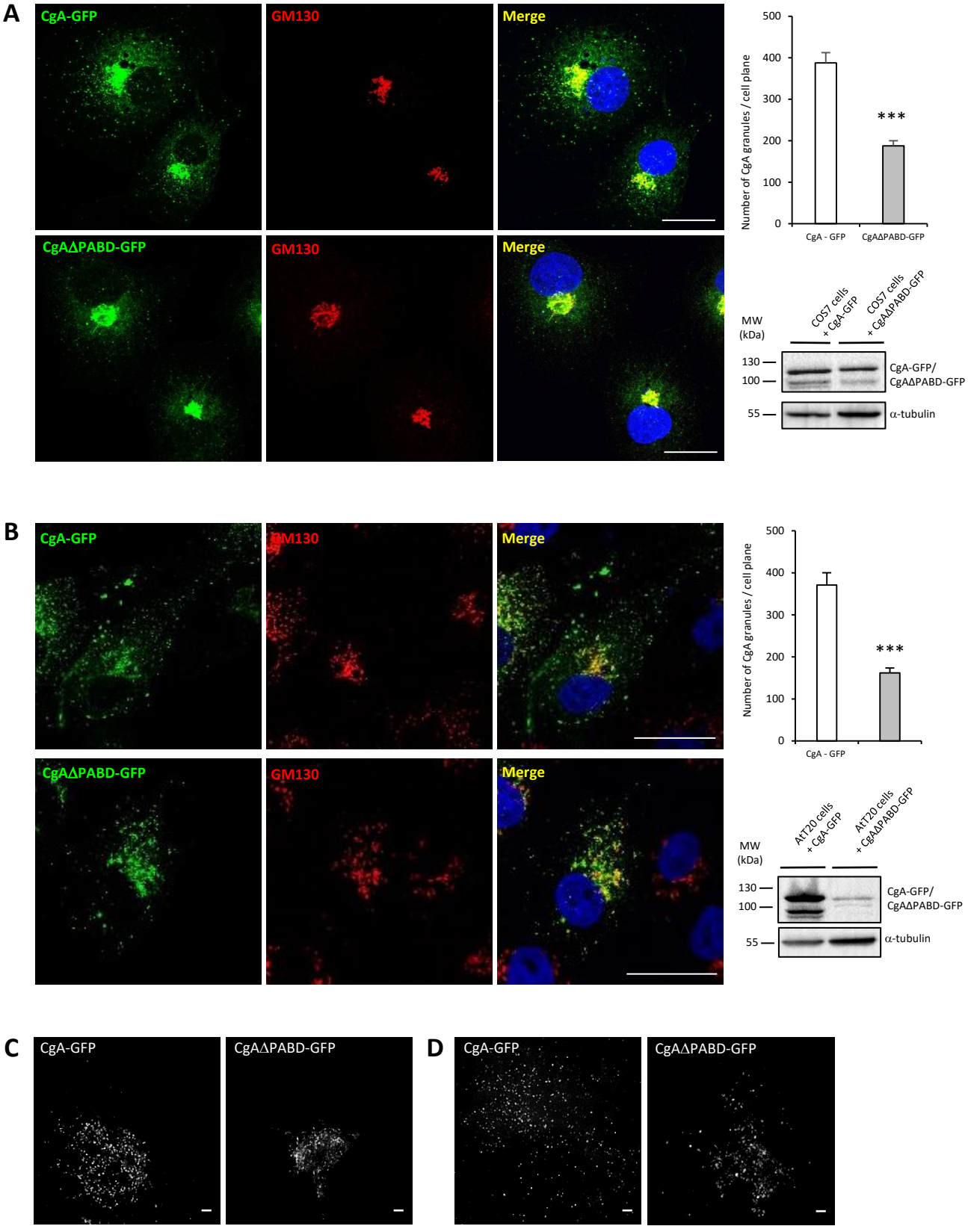

Figure 7

Figure 8

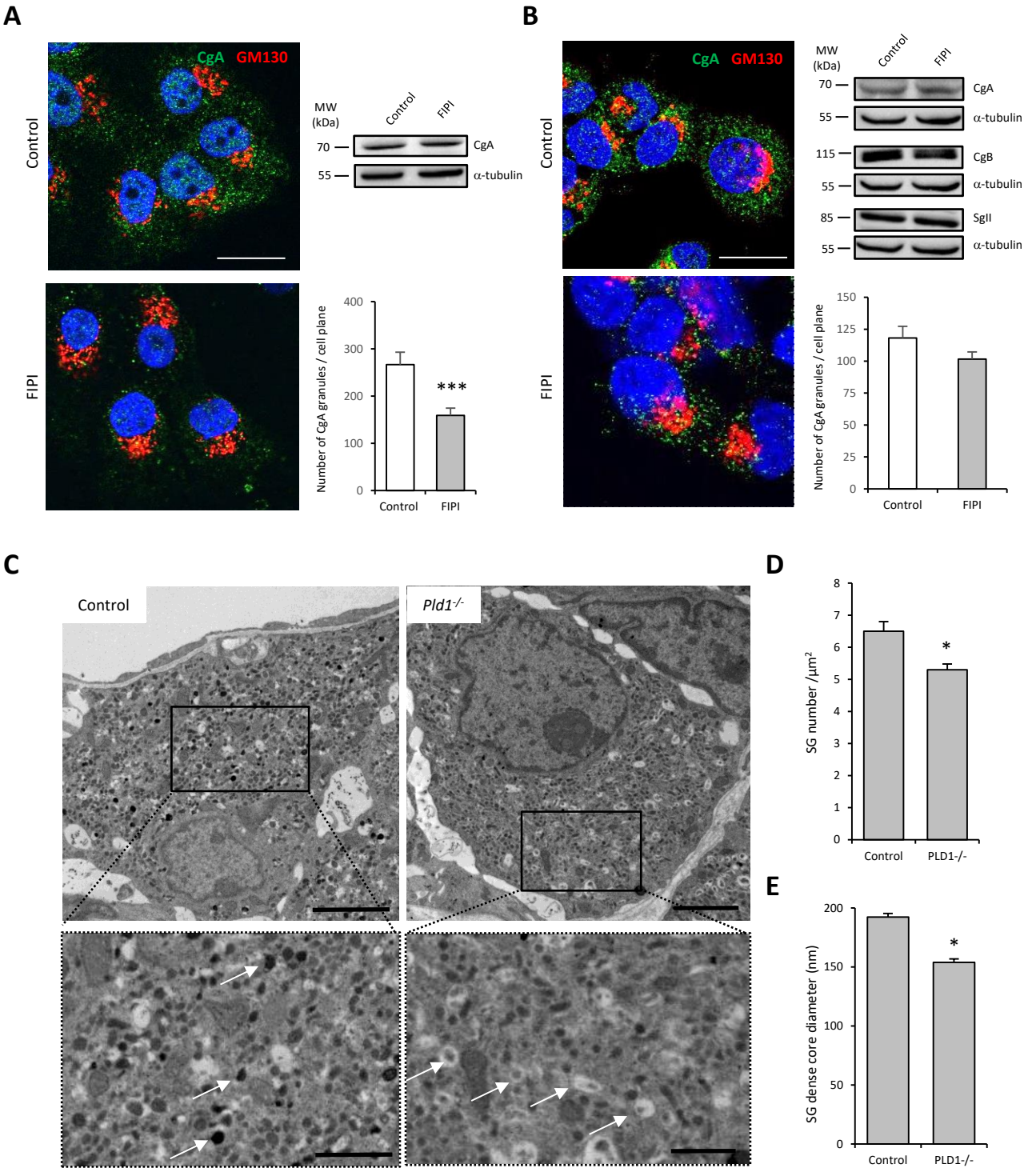

Figure 8

SUPPLEMENTAL LEGENDS

Supplemental figure 1.

A Enrichment of secretory granule membranes from COS7-CgA cells by subcellular fractionation using centrifugation on sucrose gradient. Each fraction was collected and analyzed using SDS-PAGE and SG antibody (anti-RV29.4(CgA), 70 kDa). Surrounded fraction was selected for lipidomic analysis.

B Enrichment of Golgi membranes from COS7 and COS7-CgA cells by subcellular fractionation using centrifugation on sucrose gradient. Each fraction was collected and analyzed using SDS-PAGE and immunobloting with antibodies raised against ER (anti-CALR, 70 kDa), mitochondria (anti-GLUD1, 55 kDa), *cis*-Golgi (anti-GM130, 130 kDa), and *trans*-Golgi (anti-golgin 97, 97 kDa). Surrounded fractions were selected for lipidomic analysis.

Supplemental figure 2. Imaging of CgA-GFP positive vesicles in fixed COS7 cells through confocal light scanning microscopy (CLSM) (A) and deconvoluted time-gated STED nanoscopy (STED + Deconvolution) (B). While GFP-CgA-positive structure is described as a single object through CLSM, "STED + Deconvolution" approach reveals the existence of two vesicles (blue arrows). (C) Improvement of lateral resolution (full width at half maximum, FWHM) and signal to noise ratio (SNR) through "STED + Deconvolution" strategy. An intensity profile was measured along a segment drawn on ten vesicles (yellow arrows) and diameter was determined at full width at half maximum (FWHM). Noise (blue squares) and Signal (red circles) were measured in 5 different positions in (A) and (B). Through "STED + Deconvolution" strategy, vesicle diameter is divided by three and SNR is increased sixfold. (D) Graphic representation of the increase in lateral resolution obtained through "STED + Deconvolution" strategy. An intensity profile was measured along a segment and adjusted by using a Gaussian fit. While CgA-GFP positive structure is described as a single object through CLSM (broken line), "STED + Deconvolution" approach reveals the existence of two vesicles (full line).

Supplemental video 1. Distribution of fluorescence around DOPC/PA/PE-NBD GUVs before CgA addition is homogenous. Confocal live-cell imaging of GUVs containing PE-NBD (green) was registered over a period of 1 min. Still images are shown in Fig. 3C.

Supplemental video 2. Distribution of fluorescence concentration before membrane deformation of DOPC/PA/PE-NBD GUVs triggered by 2 µM CgA addition is not homogenous. Confocal live-cell imaging of GUVs containing PE-NBD (green) was registered over a period of 1 min. Still images are shown in Fig. 3D.

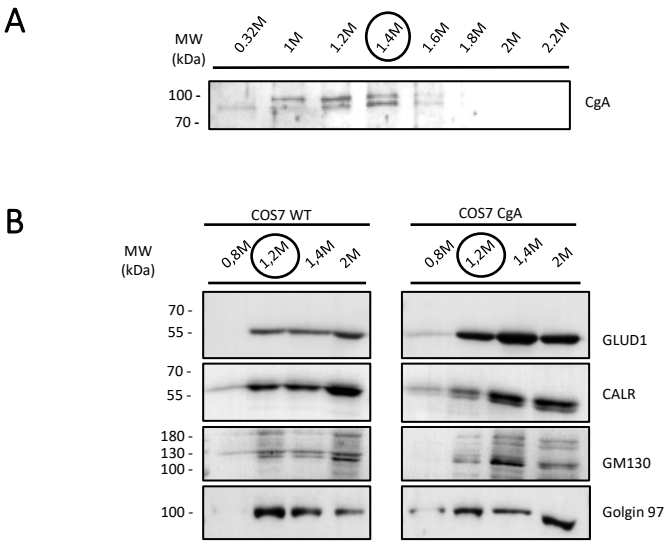
A
MW
(kDa)
0.32M
1M
1.2M
1.4M
1.6M
1.8M
2M
2.2M
100 -
70 -
CgA
B
COS7 WT
COS7 CgA
MW
(kDa)
0,8M
1,2M
1,4M
2M
70 -
55 -
GLUD1
CALR
180 -
130 -
100 -
GM130
Golgin 97

Figure S1

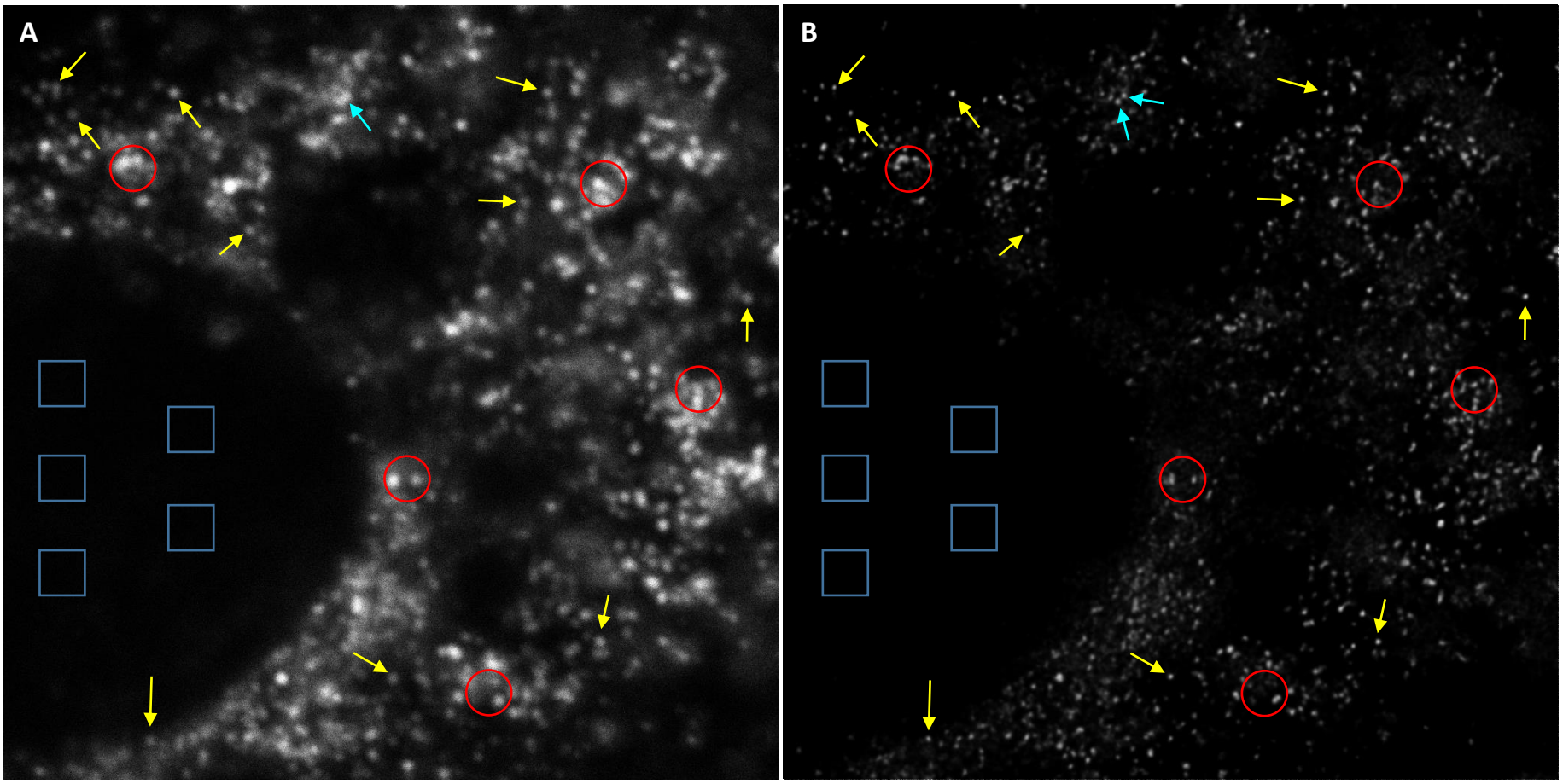

C

	FWHM (nm)	SNR = Signal / Noise
CLSM	230 ± 17	38 ± 5
STED + Deconvolution	80 ± 9	226 ± 6

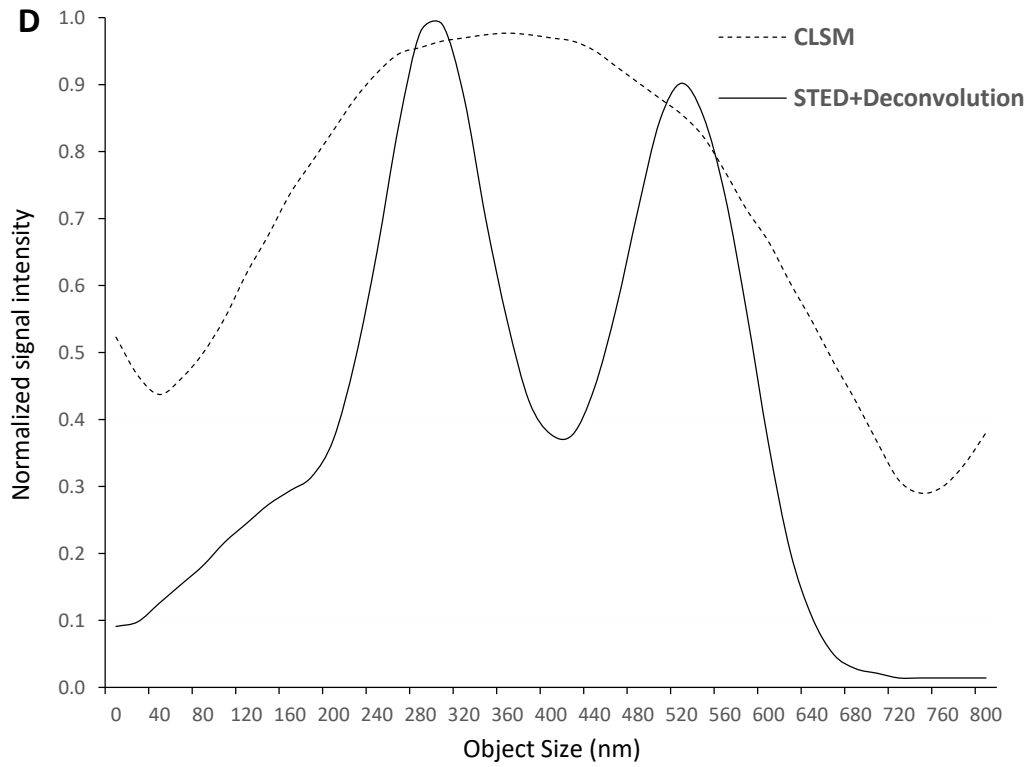

Figure S2